The mid Holocene sea-level change in the Arabian Gulf

Journal:	*The Holocene*
Manuscript ID	HOL-22-0048.R1
Manuscript Type:	Paper
Date Submitted by the Author:	10-Jun-2022
Complete List of Authors:	Mauz, Barbara; University of Liverpool, Department of Geography Shen, Zhixiong; Coastal Carolina University, Alsuwaidi, Mohammad; Khalifa University Melini, Daniele; Istituto Nazionale di Geofisica e Vulcanologia Spada, Giorgio; Urbino University "Carlo Bo" Purkis, Sam; University of Miami
Keywords:	sea-level highstand, carbonate facies, glacio-isostatic adjustment, prograding shoreline, biostabiliser, carbonate ramp
Abstract:	The mid-Holocene sea-level highstand is a well-known phenomenon in sea-level science, yet the knowledge on the highstand's spatial and temporal distribution remains incomplete. Here we study the southwest coast of the Arabian-Persian Gulf where a mid-Holocene sea-level highstand and subsequent sea-level fall may have occurred due to the Earth crustal response to meltwater load. Sea-level indicators were established using standard facies analysis and error calculations, then constrained through glacio-isostatic adjustment (GIA) modelling and though procedures based on Gaussian Process and exponential decay analysis. This work allowed to identify the highstand at 1.6±0.4 m occurring 6.7 – 6.0 ka, in excellent agreement with GIA model results. The subsequent shoreline migration followed the geophysical constraint by prograding in line with the sea-level fall until around 3 ka. Then, the strength of the external control weakened and internal processes, in particular sediment binding through microbial activity, started controlling the geometry of the accommodation space.

The mid Holocene sea-level change in the Arabian Gulf

Barbara Mauz[1,2], Zhixiong Shen[3], Mohammad Alsuwaidi[4], Daniele Mellini[5], Giorgio Spada[6], Sam J. Purkis[7]

[1] School of Environmental Sciences, University of Liverpool, Liverpool, L69 7ZT, UK
[2] Department of Environment and Biodiversity, University of Salzburg, Salzburg, 5020, Austria
[3] Department of Marine Science, Coastal Carolina University, SC 29528, USA
[4] Khalifa University, Department of Earth Sciences, Abu Dhabi, United Arab Emirates
[5] Istituto Nazionale di Geofisica e Vulcanologia, Roma, 00143, Italy
[6] Dipartimento di Fisica e Astronomia (DIFA), Università di Bologna, Bologna, Italy
[7] Department of Marine Geosciences, RSMAS, University of Miami, USA

Abstract

The mid-Holocene sea-level highstand is a well-known phenomenon in sea-level science, yet the knowledge on the highstand's spatial and temporal distribution remains incomplete. Here we study the southwest coast of the Arabian-Persian Gulf where a mid-Holocene sea-level highstand and subsequent sea-level fall may have occurred due to the Earth crustal response to meltwater load. Sea-level indicators were established using standard facies analysis and error calculations, then constrained through glacio-isostatic adjustment (GIA) modelling and though procedures based on Gaussian Process and exponential decay analysis. This work allowed to identify the highstand at 1.6±0.4 m occurring 6.7 – 6.0 ka, in excellent agreement with GIA model results. The subsequent shoreline migration followed the geophysical constraint by prograding in line with the sea-level fall until around 3 ka. Then, the strength of the external control weakened and internal processes, in particular sediment binding through microbial activity, started controlling the geometry of the accommodation space.

1 Introduction

The Holocene sea-level history is of interest because, for this time period, high-resolution data are available to reliably constrain geophysical models which describe the response of the Earth and the oceans to deglaciation. From both geophysical models and proxy data, it is well-known that the sea level in the Holocene rose above its modern elevation in certain coastal areas, after the melting of the biggest ice sheet (Laurentide) has ceased (Mitrovica and Peltier, 1991). This 'overshoot' was attributed to the interplay between equatorial ocean syphoning and 'continental levering' (Mitrovica and Milne 2002). The geophysical mechanisms controlling the mid Holocene sea-level highstand are thus well-understood, but our knowledge on the highstand's spatial and temporal distribution remains incomplete (Woodroff and Horton, 2005). Here we aim to contribute to this incomplete knowledge by investigating the southwest coast of the Persian-Arabian Gulf (hereafter "Arabian Gulf'). The coast of the Arabian Gulf has been studied extensively (e.g., Kendall and Alsharhan 2011) and all these studies agreed that a sea-level highstand must have occurred at around 6 ka (e.g., Lokier et al., 2015; Parker et al., 2020; Engel et al., 2021). Yet, the exact elevation of the highstand and the response of the coast to the subsequent sea-level fall is still unclear. Our objective is therefore to close this data gap by establishing sea-level proxy data for the shoreline position. This position is likely controlled by the Earth's crustal response to meltwater load as well as by local processes such as carbonate productivity, hydrodynamically induced erosion and geometry of accommodation space. If the spatio-temporal distribution of the proxy data is mainly externally controlled, the proxies reflect the Arabian Gulf's crustal response to meltwater load. If the proxies do not follow the modelled response to the melting of ice sheets, then it can be assumed that internal controls dominate the indicative meaning of the proxies, hence the shoreline position. We show here that proxy data require additional analytical treatment to reliably quantify the geophysically-induced signal.

2 The study area

The Arabian Gulf (Fig. 1) is part of the Arabian plate characterised by topographic asymmetry with high elevations in the west and surface dipping to the east where the Gulf forms a foredeep basin dipping towards the north-eastern Zagros Mountains. The plate's crust and, most likely also the lithospheric mantle, thickens to the east leading to an overall lithospheric thickness of ~160 km beneath the foredeep basin of the Gulf (Stern and Johnson, 2010). The Gulf is an epicontinental sea separated from the Indian Ocean by the Strait of Hormuz where the water depth of the sill is ~80 m (Bower et al., 2000). The annual mean water volume transport at the Strait is relatively small (Bower et al., 2000) suggesting that the flooding of the basin in deglacial times occurred at a slow pace. The average water depth in the Gulf is today 35 m and reaches around 100 m near the entrance at the Strait. The sea-water current in the Gulf is anti-clockwise from the Strait of Hormuz with highest salinity (dense water) in the southwest (Alsharhan and Kendall 2003).

[insert Figure 1.]

Sites suitable for studying the Holocene sea-level history are situated on the western and southern coast of the Gulf which exhibits tectonic quiescence and absence of sediment disturbances such as compaction and unsuitable sedimentation rate. We investigated (1) Al Khidayrah and (2) Mussafah Channel and studied literature on (3) North Qatar and (4) Ghagha island (Fig. 1).

On the SW coast, diurnal and mixed tidal regimes dominate with tidal ranges of 1.0 - 1.5 m in protected zones (e.g., lagoon) and ~2.5 m on open coasts (Alsharhan and Kendall, 2003). Mean spring tide is 1.1 m and mean neap tide is 0.75 m, modified by diurnal inequality and occasional strong winds.

2.1 Coastal sediments

The study area is part of the Arabian Gulf's homoclinal carbonate ramp (Read 1985), the geometry and topography of which is a result of the eastward dipping foredeep basin and the carbonate factory. This factory operates year-round with 10-100 mm/a sedimentation rate (Reijmer, 2021) resulting in a flat-topped platform geometry with a steep slope at ~40 m water depth (Park, 2011). In the protected coastal zones behind barrier islands, the typical lateral sedimentary succession of the inner ramp is composed of low-lying sabkhas and their evaporitic components (e.g., anhydrite) in places overlain by beach ridges; this is seaward followed by algal and microbial mats, mangrove mud, carbonate sand and silt and hardground (see Figs S1 and S2 for upper intertidal and hardground). On the open coast, the sabkha is seaward followed by oolitic or skeletal sand and coral reefs (Purkis and Riegl, 2005). The coast is therefore an evaporitic factory gradually transforming seaward into a carbonate factory where seasonally blowing strong winds influence the distribution of the carbonate facies.

The carbonate factory is dominated by bio-chemically induced precipitation of mud and peloids and by skeletal components (calcareous algae, foraminifera, bryozoans). On the inner ramp, benthic microbial communities typically dominated by cyanobacteria dominate the factory. They secrete extracellular polymeric substances (biofilm) which trap and bind sediment and organic matter (Suarez-Gonzales et al. 2019). The mats are biostabilisers, thereby contributing to the factory's capacity to build fast-prograding sediment bodies (Reijmer, 2021, Williams et al., 2011). Besides these mats, the second important component of the inner ramp is hardground which forms in the inter- to subtidal through precipitation of carbonate minerals on the surface of carbonate particles supported by algal filaments (e.g., Christ et al., 2015; Ge et al., 2020). The flat pavement formed by hardground is widespread in water depth <2 m but also occurs in deeper water where it provides settlement substate for corals (Purkis et al., 2011). Carbonate sand and silt, represented by grain- and packstone facies is the typical product of the factory filling tidal creeks and channels as well as pools between microbial mats. The unconsolidated material is swept by tidal currents, hence transported in and out of the inner ramp. On the Gulf's arid coast, beachrock forms in the supratidal zone through evaporation of sea-water spray and episodically occurring rainwater in the pores of the carbonate sand.

The spatial distribution of the nearshore facies relevant for sea-level reconstruction is not the same everywhere but exhibits variable relationships to water depth. The patterns displayed in Figs 2 and 3 exemplify the ongoing debate about facies distribution on carbonate platforms: the distribution may follow patterns such as belts (e.g., Burchette and Wright, 1992), mosaics (Wright and Burgess, 2005), scale-invariant fractals (Schlager, 2004; Purkis et al., 2005; Purkis and Kohler, 2008) or it follows a power-law relationship (Purkis et al., 2005).

2.2 The Holocene sea-level highstand in the Arabian Gulf

The carbonate ramp and, in particular the coast around Abu Dhabi, has been studied frequently (e.g., Evans, 2011; Shinn, 2011; Kirkham and Evans, 2020) and in great detail (e.g., Purkis et al., 2005; Strohmenger et al., 2011). All these studies agreed that a mid-Holocene sea-level highstand occurred at 2-3 m (Strohmenger et al., 2010) or at ca 1 m (Lokier et al., 2015). For the Euphrates-Tigris delta Aqrawi (2001) found a mid-Holocene marine intrusion lasting around 2 ka. For the western coast Parker et al. (2020) found the highstand at ca 2.4 m occurring around 6.9 ka. For the north coast of the Qatar Peninsula Rivers et al. (2020) found the highstand at 1.6 m lasting around 2 ka (7-5 ka). Lambeck (1996) studied the Holocene shoreline migration using his glacio-isostatic adjustment (GIA) model and predicted a 3.5 m highstand occurring on the SW-coast of the Gulf.

3 Methods

The methodological approach assumes that the sea-level indicator carries the signature of externally and internally induced processes. The external control is exerted by GIA-induced processes and the internal control is induced by local processes such as hydrodynamics, carbonate productivity and microbial activity. The indicator provides proxy data for the spatio-temporal distribution of the shoreline position. The indicator is primarily controlled externally if its proxy data follow the GIA prediction, but controlled internally if its proxy data deviate from the prediction. The indicator is converted to a sea-level index point (SLIP) through (i) accurate and precise elevation data including error estimation, (ii) calibrated radiocarbon age and (iii) detailed lateral and vertical facies description to infer indicative meaning and indicative range of the dated deposit (for lateral and vertical facies descriptions, and related indicative meaning, see Fig. 4. For calculation of SLIP, see supplement.)

3.1 Field survey and elevation

To survey modern coastal facies, field work targeted artificial outcrops ('SH' in Fig. 3A inset) at the modern shoreline. To relate this with buried coastal facies pits were dug in beach ridges. All sites including the Mussafah Channel (MC) site (Fig. 3; Kirkham, 1998; Strohmenger et al., 2010) were measured using dGPS levelled to benchmark ID 3197 (Abu Dhabi). Sampling focused on hardgrounds for thin section analysis and on intertidal carbonate sand for XRF and radiocarbon analyses. In a subsequent field visit data and the facies interpretation was tested and verified.

3.2 Facies analysis

To determine the indicative meaning of each sea-level indicator the modern analogue of facies distribution was established. For this purpose, results from field survey and logging and from x-ray fluorescence (XRF) analysis (see supplement for details) were compared and complemented with data from literature for the purpose of facies description. Nearshore facies distribution was mapped from Google Earth images and the geological map of Alsharhan and Kendall (2003).

3.3 Glacio-isostatic adjustment modelling

To quantify the external control on sea-level indicators, past sea-level history was modelled by obtaining a set of high-resolution numerical solutions of the Sea-Level Equation using the SELEN4 solver (Spada and Melini, 2019). Each numerical solution was computed on a global icosahedon-based grid with spacing of ~40 km. It accounts for spectral terms up to harmonic degree L=512 corresponding to a wavelength of ~78 km on the Earth's surface. The boundary conditions for paleo-topography are prescribed through the ETOPO1 global topographic model (Amante and Eakins, 2009), integrated with the Bedmap2 relief (Fretwell et al., 2003) of the Antarctic region. Three global GIA models were used, i.e., ICE-6G (Peltier et al., 2015), ICE-7G (Roy and Peltier, 2015, 2017) and one of the models progressively developed by the Kurt Lambeck group at the Australian National University (ANU, e.g., Nakada and Lambeck, 1987; Lambeck et al., 2003). For each model run the nominal rheological profile and a modified profile was implemented where the modified profile used a lithospheric thickness (LT) of 160 km indicated by Stern and Johnson (2010) for the eastern portion of the Arabian plate.

3.4 Modelling proxy data

Most of the SLIPs established cover the sea-level fall subsequent to the mid-Holocene highstand. This fall should be controlled by the crustal response to water load (Mitrovica and Milne 2002) with minor contribution of additional meltwater. To identify the internal control on SLIPs, all those proxy data that indicate sea-level fall were fitted using the exponential decay function of the form $y=a*e^{(-x/t)}+y_0$ where a and y_0 stand for amplitude and offset, respectively, and 1/t represents the decay rate. This type of decay function is prescribed by the shape of the sea-level curves obtained from the GIA models for the period ca 6-0 ka when sea level falls (Fig. S3). In addition, the proxy data-distribution was modelled using a Gaussian process (GP) model for the period 4-0 ka. The GP model runs with seven hyperparameters (prior standard deviations) representing fast (decadal scale) and slow (centennial scale) changes of global sea level, fast and slow changes of sea level on local and regional scales, and a regionally varying linear hyperparameter for a GIA process deduced from ICE 5G(VM2-90). For details of the model see Kemp et al. (2018). After a test run for individual sites which returned insignificant difference between sites, the SLIP data were combined to one virtual site.

3.5 Sea level and shoreline analysis

Because the sea-level indicators provide proxy data for the shoreline position, we compare the rate of sea-level fall with the rate of shoreline progradation. It is expected that the shoreline migrates at a rate lower than the size of the accommodation space changes, because the year-round operating carbonate factory remains unaffected by the geophysical process governing the sea-level change. The shoreline migration is calculated using the well-defined location of the MC site (Fig. 3A) which is 8 km away from the present-day mean shoreline (Kirkham, 1998). The slope angle of the inner ramp is 0.07° (Lokier et al 2018) or, in some areas, it is 0.05° to 0.06° or 0.48° and 0.53° (Court et al., 2017; see also 3D model of this ramp in Purkis et al., 2005). Using a linear regression line with *x* being the distance between the MC site and the modern shoreline and the slope resulting from tan(α), where α=0.07° or α=0.04°, the shoreline progradation is calculated for the period 6.7 – 0 ka. The approach assumes that over the small temporal scale of interest here, the slope angle at a given location is constant. The rate of sea-level change was deduced from the exponential fit of the proxy data.

3.7 Uncertainties

The generation of sea-level data includes uncertainties arising from measurements (elevation, dating) and models, and also from facies analysis. The latter represents the uncertainty of water-depth attribution to a dated sea-level indicator. For biotic indicators (e.g., corals) this is the living range and, for bio-chemically induced deposits, it is the water-depth range of a given facies. Because the carbonate factory studied here is a bio-chemical system with variable spatial distribution of biostabilisers, the deterministic approach 'one facies, one water depth' (e.g., Purkis et al., 2015), hence indicative range, is likely inappropriate to capture the true indicative range. Equally, the summing in quadrature of error terms seems insufficient to capture the true variability of the water depth. On the other hand, including all possible water depths into the error term of a given facies and propagating this alongside other errors, the resulting effective uncertainty would render the associated value meaningless. Here, we use the standard procedure of error calculation for individual data points (Hijma et al., 2015), but take the uncertainty of the highstand elevation from the 95% confidence level (CL) of the exponential fit (see Fig. S4 for CL).

4 Results

4.1 Sedimentary facies and indicative meaning

On the barrier island coast (Abu Dhabi) the sedimentary succession relevant for Holocene sea-level assessment starts with microbial mat or hardground (Fig. S5A and C) situated around 1– 2 m above modern sea level. On the north Qatar coast it starts with intertidal carbonate sand or reef mounds overlying Eocene bedrock (Fig. S5B). It follows 1-2 m thick carbonate fine sand represented by intertidal skeletal grainstone, packstone or laminated fine sand characterised by Ca/Si ~20 and Ca/Sr ~70 (Fig. S6A). The supratidal is represented by bioclastic sand, anhydrite and halite- or gypsum crust reflected by high calcium and sulphate percentages in the sediment (Fig. S6B). On the coast behind barrier islands sediment successions are dominated by tidal channel facies (Fig. S5C). The Holocene flooding surface is carved into bedrock (Qatar) or it is a hardground (Abu Dhabi) characterised by granular texture (for details of hardground facies see Fig. S2 and Table S1). On Ghagha island the succession is composed of Neogene limestone overlain by bioclastic sand in places cemented to beachrock.

The modern coastal sedimentary environment shows a facies distribution of evaporitic anhydrite or halite-gypsum mud and bioclastic sand in the supratidal, carbonate sand, algal- and microbial mats, hardground and reef mounds in the inter- to subtidal. Modern facies distribution appears to be random on the open coasts of north Qatar (Fig. 2) and appears to follow belts on small scale (Fig. 3).

[insert Figure 2.]

[insert Figure 3.]

4.2 Proxy data

On the basis of lateral and vertical facies distribution the modern analogue facies model (Fig. 4) provides the relative water depth of facies, hence indicative meaning and range of sea-level indicators.

[insert Figure 4.]

The modern analogue of facies distribution (Figs 2, 3, 4) together with the established requirements for sea-level indicators result in 22 SLIPs providing proxy data points for former shoreline positions (Table 1; for details of data see supplement).

Table 1. Proxy data generated in this study. Reference water level is mean sea level for all samples. For details see supplement.

Site	Sample	Lat	Long	Elevation (m)	Age (ka cal BP)	IR (m)	Palaeo mean sea level	Indicator	Reference
Al Khidayrah	SH1R	24.11	54.06	1.35±0.03	2.87±0.35	0.38±0.19	0.97±0.19	Carb sand; SLIP	This study
Al Khidayrah	SH2R	24.11	54.05	1.35±0.03	2.79±0.37	0.38±0.19	0.97±0.19	Carb sand; SLIP	This study
Al Khidayrah	SH7L	24.10	54.07	2.20±0.04	6.26±0.37	1.00±0.50	1.20±0.50	Beach ridge; SLIP	This study
Al Khidayrah	SH7U	24.10	54.07	2.50±0.04	5.67±0.38	1.40±0.70	1.10±0.70	Beach ridge; t SLIP	This study
Al Khidayrah	SH6U	24.10	54.06	2.26±0.03	4.26±0.42	1.40±0.70	0.86±0.70	Beach ridge; SLIP	This study
Al Khidayrah	SH6L	24.10	54.06	1.94±0.03	4.58±0.42	1.00±0.50	0.94±0.50	Beach ridge; SLIP	This study
Mussafah	MC1-4	24.31	55.29	2.15±0.03	6.35±0.41	0.55±0.27	1.61±0.27	Microbial mat; SLIP	Strohmenger et al., 2010
Mussafah	MC2-2	24.31	55.29	2.22±0.03	6.80±0.43	0.55±0.27	1.68±0.27	Microbial mat; SLIP	Strohmenger et al., 2010
Mussafah	MC3A-2	24.31	55.29	1.75±0.03	6.30±0.42	0.55±0.27	1.21±0.27	Microbial mat; SLIP	Strohmenger et al., 2010
Mussafah	MC3A-7	24.31	55.29	2.65±0.03	5.78±0.46	0.70±0.35	1.95±0.35	Hardground; SLIP	Strohmenger et al., 2010
Mussafah	MC4-2	24.31	55.29	1.90±0.03	6.79±0.43	0.55±0.27	1.36±0.27	Microbial mat; SLIP	Strohmenger et al., 2010
North Qatar	C1-1	26.15	51.27	0.13±0.02	5.81±0.12	1.20±0.60	1.33±0.60	Carb sand; SLIP	Rivers et al., 2020
Al Ruwais	C4-1	26.14	51.27	-0.13±0.02	6.06±0.15	1.80±0.90	1.07±0.90	Carb sand; SLIP	Rivers et al., 2020
Al Ruwais	C4-2	26.14	51.27	0.02±0.02	6.73±0.16	1.80±0.90	1.22±0.90	Carb sand; SLIP	Rivers et al., 2020
Al Ruwais	C4-3	26.14	51.27	0.82±0.02	5.75±0.14	1.80±0.90	2.02±0.90	Carb sand; SLIP	Rivers et al., 2020
Al Ruwais	C4-4	26.14	51.27	0.84±0.02	5.98±0.17	1.80±0.90	2.04±0.90	Carb sand; SLIP	Rivers et al., 2020
Um Tays Island	C5-1	26.16	51.28	-2.84±0.02	3.90±0.17	2.50±1.25	-1.64±1.25	Reef; SLIP	Rivers et al., 2020
Um Tays Island	C5-2	26.16	51.28	-2.60±0.02	3.66±0.16	2.50±1.25	-1.40±1.25	Reef; SLIP	Rivers et al., 2020

Ghagha island	G03	24.41	51.55	2.43±0.24	6.31±0.11	1.50±0.75	1.55±0.79	Beachrock; SLIP	Arhan et al., 2020
Ghagha Island	Ge2	24.41	51.55	2.87±0.29	5.88±0.14	1.00±0.50	1.99±0.58	Beachrock; SLIP	Arhan et al., 2020
Ghagha Island	Ge1	24.41	51.55	1.67±0.17	3.30±0.26	1.00±0.50	0.79±0.53	Beachrock; SLIP	Arhan et al., 2020
Khawr Qantu	Site01-B39	24.12	54.03	-0.0205± 0.0008	1.24±0.35	0.55±0.27	0.53±0.27	Microbial mat; SLIP	Lokier and Steuber, 2008
Khawr Qantu	Site10-S143	24.12	54.01	-0.275± 0.011	0.46±0.31	0.55±0.27	0.27±0.27	Microbial mat; SLIP	Lokier and Steuber, 2008

4.3 GIA

The sea-level curves simulated by the ICE-7G and ANU models are similar in terms of trend and timing of the sea-level highstand (Fig. 5). The ICE-7G model predicts a highstand that is around 0.8 m higher than the one predicted by ANU. For the time 6-0 ka both curves follow a single exponential decay with ICE-7G being almost identical (χ^2_{red}=0.00036) to this fitting function (Fig. S3).

[insert Figure 5.]

4.4 Proxy data and model results

The sediment succession in the MC site (Fig. S5C) indicate increasing water depth between microbial mat and upper hardground. The mid-Holocene microbial mats are therefore part of the transgressive phase with the maximum transgression surface indicated by the upper hardground. All other proxies reflect the falling sea level occurring subsequent to the highstand. Proxy data derived from intertidal carbonate sand, beachrock, microbial mats and hardground deliver variable elevations but are consistent within error margins. Proxy data derived from beach ridges plot consistently around 0.7 m and those derived from the reef plot around 2 m below the predicted elevation. In the MC site the highstand is indicated by the hardground at 2.0±0.4 m and 5.8±0.5 ka (Fig. S5C).

The curve resulting from the exponential (exp) fit of the proxy data (Fig. S4) is flat-angle and curved compared to the curves derived from the GIA models (Fig. 6). The negative curvature is dictated by the data points representing the period 3-0 ka. The exp proxy curve indicates the highstand to occur at 1.6±0.4 m around 6.7 ka. The ANU model indicate the highstand at 2.0 m and the ICE-7G predicts the highstand to occur at 2.8 m. Both GIA models predict the highstand for the time around 6 ka.

The GP-modelled curve falls from around 1 m to zero, which is the trend indicated by the proxy data.

The shape of the curve follows the global sea-level function implemented in the GP model with negligible contribution from the local sea-level component (Fig. S10).

[insert Figure 6.]

4.5 Sea level and shoreline

On the inner carbonate ramp the shoreline prograded since 6.7 ka downslope between around 10 m (slope angle 0.07°) and around 6 m (slope angle 0.04°) (Fig. 7). The sea level fell at the same time from 1.6 m to zero meter. Where the slope angle is 0.07° the shoreline migrated almost in pace with the sea-level; on slopes with <0.07° angles the shoreline's progradation is reduced.

[insert Figure 7.]

5 Discussion

5.1 Indicative meaning and quality of proxy data

In this study sea-level indicators selected for the purpose of sea-level reconstruction were intertidal microbial mats, hardground and carbonate sand, subtidal coral reef and supratidal beachrock and beach ridges. The N-Qatar coast sea-level indicators were derived from intertidal carbonate sand and *in situ* coral remains (Rivers et al., 2020). With a tidal range of 1.1 m (up to 2.3 m) the flooding surface must be -1 m at 4 ka to reconstruct a highstand of approximately 2 m, but the surface is at -3 m and, consequently, the reef-derived proxy data plot below the expected sea-level. It is possible that the Eocene bedrock surface was carved during the LGM lowstand and was colonised during deglacial sea-level rise by a coral assemblage for which the bedrock surface was situated within its living range (e.g., Riegl and Purkis, 2012 for living range of corals). For the Ghagha island coast sea-level indicators were derived from beachrock (Arhan et al., 2020) which is a reliable indicator for the supratidal zone due to the immediate lithification of the beach sand. For the Abu Dhabi barrier island coast intertidal microbial mats, carbonate sand and hardground are indicators of variable reliability. Microbial mats seem to be more linearly related to water depth in protected zones behind barrier islands (Fig. 2) but on the open coast east of Abu Dhabi they can colonise sandy substrates almost everywhere in the intertidal to upper subtidal zone (Purkis et al., 2005). It appears that the microbial mats grow to a thickness that can withstand high-energy waves and currents in protected zones where they have time to the develop the biofilm (Mariotti and Fagherazzi, 2012). Thus, on the inner carbonate ramp it is the absence of high energy rather than the water depth that controls the occurrence of the mats.

Carbonate sand is mostly unconsolidated, hence mobile and easily swept by tidal currents. In fact, the variable vertical succession of the two key stratigraphic facies, i.e., hardground and microbial mat (see Fig. S5 and Strohmenger et al., 2011) indicates a complex spatial relationship between facies. This is not reflected in the modern analogue facies model (Fig. 4) which is suggestive of a belt-shaped concept where facies are parallel to the shoreline and linearly related to water depth. The question is, therefore, whether small sea-level changes can trigger facies-belt migration or trigger extension or reduction of belts where the mean water depth of individual facies belts remains constant. Also, the water depth may be variable in places owing to the variable tides (semidiurnal to diurnal with diurnal inequalities) and to the strong winds which affect the arrival time of high and low tides and the tidal currents. The nearshore facies distribution on a carbonate ramp has been described as a mosaic (Purkis et al., 2005; Wright and Burgess, 2005; Kendall and Alsharhan, 2011) rather than belt-shaped, and this clearly impairs rigorous quantification of water depth. Moreover, some of our sea-level proxy data are obtained from the protected coast behind barriers where the facies are dominated by tidal channel deposits, indicating substantial lateral movement of unconsolidated sand including the destroying of earlier facies successions. On the other hand, the reconstructed modern analogue in Fig. 4 is a result of a decrease in accommodation space due to sea-level fall, and this is what we reconstruct in this study. We can say that our sea-level proxies determined on the basis of the modern analogue are uncertain observations of the true shoreline position. The quantitative uncertainty associated with the observation is then not noise resulting from measurements, but rather reflects our incomplete understanding of the quantified system.

5.2 Glacio-isostatic Adjustment models

The sea-level curves obtained from the two ICE models (ICE-6G and ICE-7G) are almost identical (Fig. S7) despite the different viscosity profiles (Fig. S8) employed in each model. Moreover, the output of the two models remain almost unchanged, also when the regional-scale lithospheric thickness of 160 km is used instead of the nominal value (90 km). Only the higher viscosity profile for the lower mantle seem to affect the model output as indicated by the curve obtained from ANU (Fig. 5) where the highstand is around 0.8 m lower than that predicted by the ICE models. Thus, assuming a thick lithosphere of 160 km and a high lower mantle viscosity brings the elevation of the highstand from around 3 m closer to the proxy data which suggest less than 2 m. ANU and ICE are also different in terms of the eustatic function where ANU implements continuous melting of the Antarctic until 2 ka and the ICE models assume all melting has ended by 6 ka (Fig. S9). This should affect the modelled water load in the Gulf after 6 ka, hence the shape of the simulated curve. However, the rate of sea-level change is almost identical in both GIA models for the time 6-0 ka (Fig. S11) and thus, any additional meltwater injected after 6 ka does not affect the crustal response of the eastern Arabian plate. Lambeck (1996) postulated a 3.5 m sea level for the coast between Qatar and Abu Dhabi. Without knowing all details of model parametrisation, we can only speculate that the around 1.5 m difference to our model result is owed to the rheological profile and, certainly also, to the numerical solution of the models. The timing of the highstand itself and the timing of the subsequent sea-level fall is almost identical in all predictions and some 100 years later than indicated by the proxies.

5.3 Proxy data modelling results

With the uncertain shoreline observation in mind, it cannot be assumed that individual proxies reconstruct the sea level accurately, but the assemblage of proxy data derived from the same coast experiencing the same sea-level history should deliver reliable information, subject to analytical procedures that account for the underlying processes. We have selected two analytical procedures: Gaussian Process (GP) and exponential decay. The first employs a spatio-temporal statistical analysis to decompose the local dataset of sea-level change in addition to a global one, and the second follows the geophysical constraints.

The GP-modelled curve captures the trend of the proxy data and suggests that its key assumption, that is the normal distribution of data, is valid despite the variable context of the proxies themselves. This is an astonishing result given the uncertain, potentially non-linear, observation provided by individual sea-level indicators. Both the GP-modelled curve and the exp proxy curve plot below the exp GIA curves (Fig. 6). This confirms the sea-level fall indicated by the proxy data, which is a little less than the one indicated by the GIA-curves (Fig. 6). On the other hand, the two curves diverge progressively after ca 2.5 ka. For this latter period, the exp proxy curve suggests decreasing sea-level fall, hence weakening of the external control, while the GP-modelled curve indicates no deviation from the global trend. Thus, the decreasing sea-level fall is statistically negligible, which is a logical consequence of the proxy data uncertainties treated as noise in the GP model.

The results from the GP model, the GIA models, and the exp proxy fit describe a difference in highstand elevation of 0.3-0.5 m. This difference translates to a variation in shoreline position along the slope of 250-400 m. With the width of the modern microbial mat belt being 150-800 m (Court et al., 2017) and the ability of the mats to adjust quickly to a changing accommodation space (e.g., Wu et al., 2021), we can say that the global GIA models excellently approximate the shoreline positions inferred from the proxy data.

5.4 Sea-level fall and shoreline migration

The comparison between sea level and shoreline should allow to qualitatively assess the influence of internal processes on the proxy data. The internal factors controlling the position of the shoreline are the slope angle (geometry) and the organisms which bind the sediment produced in the carbonate factory from where it is transported upslope onto the platform. The results indicate that the movement of shoreline is in line with the sea-level fall (Fig. 7), if the slope angle is 0.07°. This indicates that the inner ramp geometry was in equilibrium between reduction of accommodation space and sediment accumulation during the mid-late Holocene. In the late Holocene, when the external control on shoreline migration decreased, sediment supply may have started to dominate the progradation rate, albeit in a statistically insignificant manner. Where the slope angle is shallower, the shoreline migrated at a slower pace most probably owing to enhanced microbial activity (and therefore sediment stabilisation) on the tidal flat. We can therefore say that the shoreline migration is controlled by external forcing, as long as this forcing is strong enough to exceed the impact of internal processes on the accommodation space.

5.5 Magnitude and timing of the highstand

Following the analysis of the proxy data the sea-level highstand was at 1.6 ± 0.4 m with negligible difference to the elevations indicated by the GIA models. The highstand lasted ~6.7 – 6.0 ka as also indicated by our models. The high precision of radiocarbon dating notwithstanding, we prefer to give a "circa" timing because different calibration curves and reservoir ages (ΔR) form the basis of the ages used in this study. The chronology of the GIA models is based on IntCal09 or Marine09 with a constant reservoir age correction of 405 years (Reimer et al., 2009). Rivers et al. (2020) and Arhan et al. (2020) used Marine13 (Reimer et al., 2013) combined with ΔR=180 ± 53 (Southon et al., 2002). The reservoir age alone leads to >200 years difference in the timing of the highstand (see also Lindauer et al., 2017 for changes of ΔR during historical times).

6 Conclusions

It is a challenge to apply a deterministic approach to a carbonate ramp environment for which facies distribution is debated to exhibit linear, random/stochastic and fractal relationships to water depth. Notwithstanding potential antagonisms, our data allow to infer shoreline progradation which followed the sea-level trend clearly until the late Holocene when the strength of the geophysical process weakened. This, in addition to the excellent agreement between results from proxy data analysis and GIA models, provide confidence in current methodology of sea-level science. For the late Holocene however, when the sea level fall diminished, the quality of our data is not good enough to fully understand the interplay between external control on sea level and internal control on facies distribution and shoreline migration.

Acknowledgements

BM and MA thank Thomas Steuber (Khalifa University) for discussing details of slope profiles and shoreline migration. Sara Stuecker (University of Salzburg) helped with producing GIS maps. BM gratefully acknowledges Peter Burgess (University of Liverpool) for stimulating discussions on carbonate facies.

Author contribution

BM designed the research and wrote the manuscript. BM and MA conducted the field work and MA analysed samples and supported mapping. ZS conducted the GP modelling work and supported proxy data analysis. DM and GS conducted the GIA modelling work. SJP supported facies description and mapping and shoreline analysis. ZS, DM, GS and SJP contributed to the writing of the text.

References

Alsharhan AS and Kendall CGStC (2003) Holocene coastal carbonates and evaporites of the southern Arabian Gulf and their ancient analogues. *Earth-Science Reviews* 61: 191–243.

Amante C and Eakins BW (2009) ETOPO1 arc-minute global relief model: procedures, data sources and analysis. NOAA technical memorandum NESDIS NGDC-24. *National Geophysical Data Center, NOAA*, *10*(2009), p.V5C8276M.

Aqrawi AAM (2001) Stratigraphic signatures of climatic change during the Holocene evolution of the Tigris–Euphrates delta, lower Mesopotamia. *Global and Planetary Change* 28: 267–283, PII: S0921-8181Ž00.00078-3

Arhan D, Paplopoulos K and Fouache É (2020) Holocene relative sea-level variations and archeological implications, Abu Dhabi western region, United Arab Emirates. *Arabian Journal of Geosciences* 13, 254.

Bower AS, Hunt HD and Price JF (2000) Character and dynamics of the Red Sea and Persian Gulf outflows. *Journal of Geophysical Research* 105(C3): 6387-6414.

Christ N, Immenhauser A, Wood RA et al. (2015) Petrography and environmental controls on the formation of Phanerozoic marine carbonate hardgrounds. *Earth-Science Reviews* 151: 176-226.

Court WM, Paul A and Lokier SW (2017) The preservation potential of environmentally diagnostic sedimentary structures from a coastal sabkha. *Mar. Geol.* 386: 1–8.

Engel M, Strohmenger CJ, Peis KT et al. (2021) High-resolution facies analysis of a coastal sabkha in the eastern Gulf of Salwa (Qatar): A spatiotemporal reconstruction. *Sedimentology:* 1-32.

Evans G (2011) An historical review of the Quaternary sedimentology of the Gulf (Arabian/Persian Gulf) and its geological impacts. I*nt. Assoc. Sedimentol. Spec. Publ*. 43: 13-44.

Fretwell P, Pritchard HD, Vaughan DG et al. (2013) Bedmap2: improved ice bed, surface and thickness datasets for Antarctica. *The Cryosphere 7*(1): 375-393.

Ge Y, Lokier SW, Hoffmann R et al. (2020) Composite micrite envelopes in the lagoon of Abu Dhabi and their application for the recognition of ancient firm- to hardgrounds. *Marine Geology* 423: 106141.

Hijma MP, Engelhart SE, Tornqvist TE et al. (2015) A protocol for a geological sea-level database, in Shennan, I. et al (eds), *Handbook of sea-level research*, Wiley: 536-556.

Kemp AC, Wright AJ, Edwards RJ et al. (2018) Relative sea-level change in Newfoundland, Canada during the past ~3000 years. *Quaternary Science Reviews 201*: 89-110.

Kendall CGStC and Alsharhan AS (2011) Quaternary carbonate and evaporite sedimentary facies and their ancient analogues. *Int. Assoc. Sedimentol. Spec. Publ.* 43, Wiley-Blackwell.

Kirkham A and Evans G (2020) Carbonate sedimentation around Jebel Dhanna: models for parts of the buried Holocene sabkha sequences elsewhere along the Abu Dhabi coastline. *Carbonates and Evaporites* 35, 24.

Kirkham A (1998) A Quaternary proximal foreland ramp and its continental fringe, Arabian Gulf, U.A.E. In: Wright VP, Burchette TP (eds), *Carbonate ramps* 149. Geological Society, London, Special Publication: 15–41.

Lambeck, K, Purcell, A, Johnston, P, Nakada, M, and Yokoyama, Y, (2003) Water-load definition in the glacio-hydro-isostatic sea-level equation. *Quaternary Science Reviews* 22(2), 309–318.

Lambeck K (1996) Shoreline reconstructions for the Persian Gulf since the last glacial maximum. *Earth and Planetary Science Letters 142*(1-2): 43-57.

Lindauer S, Santos GM, Steinhof A et al. (2017) The local marine reservoir effect at Kalba (UAE) between the Neolithic and Bronze Age: An indicator of sea level and climate changes. *Quaternary Geochronology* 42: 105-116.

Lokier S and Steuber T (2008) Quantification of carbonate-ramp sedimentation and progradation rates for the late Holocene Abu Dhabi shoreline. *Journal of Sedimentary Research* 78: 423-431.

Lokier SW, Bateman MD, Larkin NR et al. (2015) Late Quaternary sea-level changes of the Persian Gulf. *Quaternary Research* 84 (1), 69–81.

Lokier SW, Court WM, Onuma T et al. (2018) Implications of sea-level rise in a modern carbonate ramp setting. *Geomorphology* 304: 64–73.

Mariotti G and Fagherazzi S (2012) Modeling the effect of tides and waves on benthic biofilms. *Journal of Geophysical Research* 117: G04010.

Mitrovica JX and Milne GA (2002) On the origin of late Holocene sea-level highstands within equatorial ocean basins. *Quaternary Science Reviews* 21: 2179–2190.

Mitrovica JX and Peltier WR (1991) On postglacial geoid subsidence over the Equatorial oceans. *Journal of Geophysical Research* 96: 20053-20071.

Nakada, M and Lambeck, K (1987) Glacial rebound and relative sea-level variations: a new appraisal. *Geophysical Journal Internationa*l , 90(1), 171–224.

Park RK (2011) The impact of sea-level change on ramp margin deposition: lessons from the Holocene sabkhas of Abu Dhabi, United Arab Emirates. *Int. Assoc. Sedimentol. Spec. Publ.* 43: 89-112.

Parker AG, Morley MW, Armitage SJ et al. (2020). Palaeoenvironmental and sea level changes during the Holocene in eastern Saudi Arabia and their implications for Neolithic populations. *Quaternary Science Reviews* 249: 106618.

Peltier WR, Argus DF and Drummond R (2015) Space geodesy constrains ice age terminal deglaciation: The global ICE-6G_C (VM5a) model. *Journal of Geophysical Research: Solid Earth* 120: 450–487.

Purkis S, Rivers J, Strohmenger C et al. (2017) Complex interplay between depositional and petrophysical environments in Holocene tidal carbonates (Al Ruwais, Qatar). *Sedimentology* 64: 1646-1675.

Purkis SJ, Renegar DA and Riegl BM (2011) The most temperature-adapted corals have an Achilles' Heel. *Marine Pollution Bulletin* 62: 246-250.

Purkis SJ, Riegl BM and Andréfouët S (2005) Remote sensing of geomorphology and facies patters on a modern carbonate ramp (Arabian Gulf, Dubai, U.A.E.). *Journal of Sedimentary Research* 75: 861–876.

Read JF (1985) Carbonate platform facies models. *AAPG Bulletin* 69: 1-21.

Reijmer JJG (2021) Marine carbonate factories: Review and update. *Sedimentology* 68: 1729–1796.

Reimer PJ, Baillie MG, Bard E et al. (2009). IntCal09 and Marine09 radiocarbon age calibration curves, 0–50,000 years cal BP. *Radiocarbon 51*(4): 1111-1150.

Reimer PJ, Bard E, Bayliss A et al. (2013) IntCal13 and Marine13 Radiocarbon Age Calibration Curves 0-50,000 Years Cal BP. *Radiocarbon*, *55*(4): 1869-1887.

Riegl BM and Purkis SJ (2012) Dynamics of Gulf Coral Communities: Observations and Models from the World's Hottest Coral Sea. In BM Riegl and SJ Purkis (eds.) *Coral Reefs of the Gulf: Adaptation to Climatic Extremes, Coral Reefs of the World* 3: 71-93.

Rivers J, Engel M, Dalrymple R et al. (2020) Are carbonate barrier islands mobile? Insights from a mid to late-Holocene system, Al Ruwais, northern Qatar. *Sedimentology* 67: 534–558.

Roy K and Peltier WR (2015) Glacial isostatic adjustment, relative sea level history and mantle viscosity: reconciling relative sea level model predictions for the U.S. East coast with geological constraints. *Geophysical Journal International* 201: 1156-1181.

Roy K and Peltier WR (2017) Space-geodetic and water level gauge constraints on continental uplift and tilting over North America: regional convergence of the ICE-6G C (VM5a/VM6) models. *Geophysical Journal International* 210: 1115-1142.

Schlager W (2004) Fractal nature of stratigraphic sequences. *Geology* 32: 185-188.

Shinn EA (2011) Interplay between Holocene sedimentation and diagenesis, and implications for hydrocarbon exploitation: return to the sabkha of Ras Umm. *Int. Assoc. Sedimentol. Spec. Publ.* 43: 133-148.

Southon J, Kashgarian M, Fontugne M et al. (2002) Marine reservoir corrections for the Indian Ocean and Southeast Asia. *Radiocarbon* 44 (1): 167-180.

Spada G and Melini D (2019) On Some Properties of the Glacial Isostatic Adjustment Fingerprints. *Water* 11: 1844.

Stern RJ and Johnson P (2010) Continental lithosphere of the Arabian Plate: A geologic, petrologic, and geophysical synthesis. *Earth-Science Reviews* 101: 29-67.

Strohmenger C, Al-Mansoori A, Al-Jeelani O et al. (2010). The sabkha sequence at Mussafah Channel (Abu Dhabi, United Arab Emirates): Facies stacking patterns, microbial-mediated dolomite and evaporite overprint. *GeoArabia* 15: 49-90.

Strohmenger CJ, Shebl H, Al-Mansoori A et al. (2011) Facies stacking patterns in a modern arid environment: a case study of the Abu Dhabi sabhka in the vicinity of Al-Qanatir Island, United Arab Emirates. I*nt. Assoc. Sedimentol. Spec. Publ*. 43: 149-182.

Suarez-Gonzales P, Benito MI, Quijda IE et al. (2019) ‘Trapping and binding’: A review of the factors controlling the development of fossil agglutinated microbialites and their distribution in space and time. *Earth-Science Reviews* 194: 182-215.

Williams HD, Burgess PM, Wright VP et al. (2011) Investigating carbonate platform types: multiple controls and a continuum of geometries. *Journal of Sedimentary Research* 81: 18–37.

Woodroffe SA and Horton BP (2005) Holocene sea-level changes in the Indo-Pacific. *Journal of Asian Earth Sciences* 25: 29–43.

Burchette TP and Wright VP (1992) Carbonate ramp depositional systems. *Sedimentary Geology* 79: 3-57.

Wright VP and Burgess PM (2005) The carbonate factory continuum, facies mosaics and microfacies: an appraisal of some of the key concepts underpinning carbonate sedimentology. *Facies* 51: 17-23.

Figures

Fig. 1. The Arabian-Persian Gulf and location of studied sites (red rectangles). Map downloaded from ETOPO Global Relief Model doi:10.7289/V5C8276M.

Fig. 2. The modern facies distribution on the tidal flat off north Qatar (modified from Purkis et al., 2017).

Fig. 3. A - The modern coast west of Abu Dhabi and location of studied sites; B - The modern facies distribution (modified after Alsharhan and Kendall, 2003).

Fig. 4. Concept of facies distribution deduced from the modern analogue displayed in Figs 2 and 3 and from literature (Alsharhan and Kendall, 2003; Strohmenger et al., 2011).

Fig. 5. Sea-level curves predicted by ICE-7G and ANU models (LT=160 km) and by the GP model compared to all proxy data.

Fig. 6. The curves resulting from the exponential decay fit (exp) of ICE-7G (blue), ANU (black) and proxy data (red; data points representing transgression excluded). Gaussian Process (GP) model curve (purple) and proxy data are also plotted. For details of fits see Figs S2 and S3.

Fig. 7. The sea-level fall (blue line) and the shoreline progradation line (orange line) since the mid Holocene calculated for the MC site. At 6.7 ka the shoreline is at 0 m elevation at the MC site and then migrates seaward over a distance of 8 km following the falling sea level.

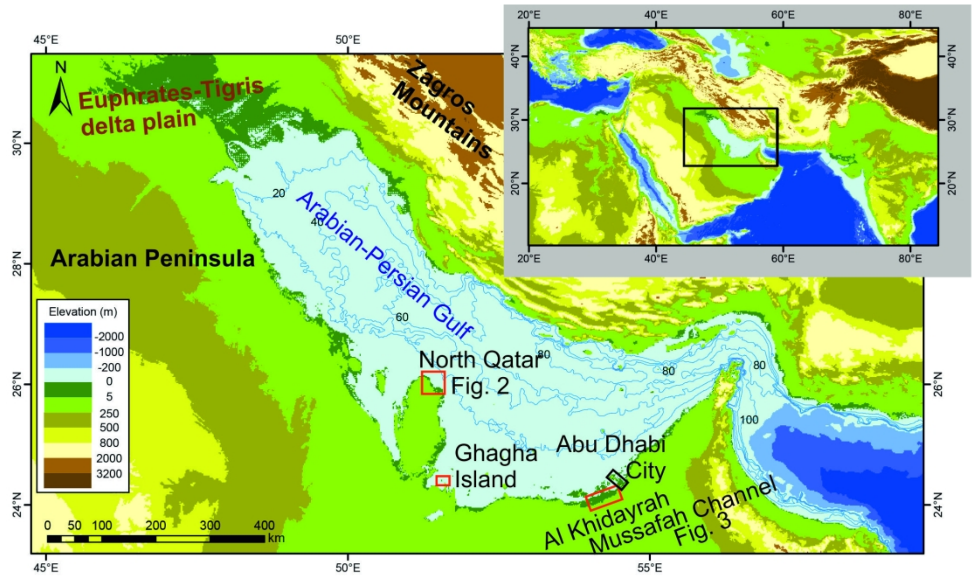

Fig. 1. The Arabian-Persian Gulf and location of studied sites (red rectangles). Map downloaded from ETOPO Global Relief Model doi:10.7289/V5C8276M.

180x103mm (300 x 300 DPI)

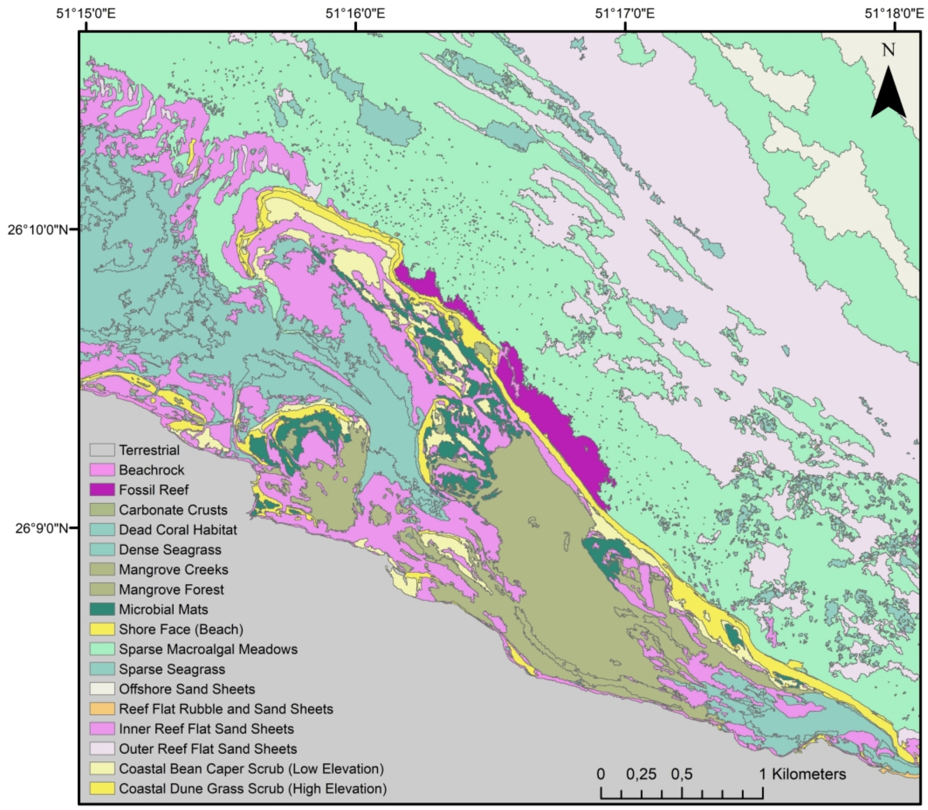

Fig. 2. The modern facies distribution on the tidal flat off north Qatar (modified from Purkis et al., 2017).

205x191mm (600 x 600 DPI)

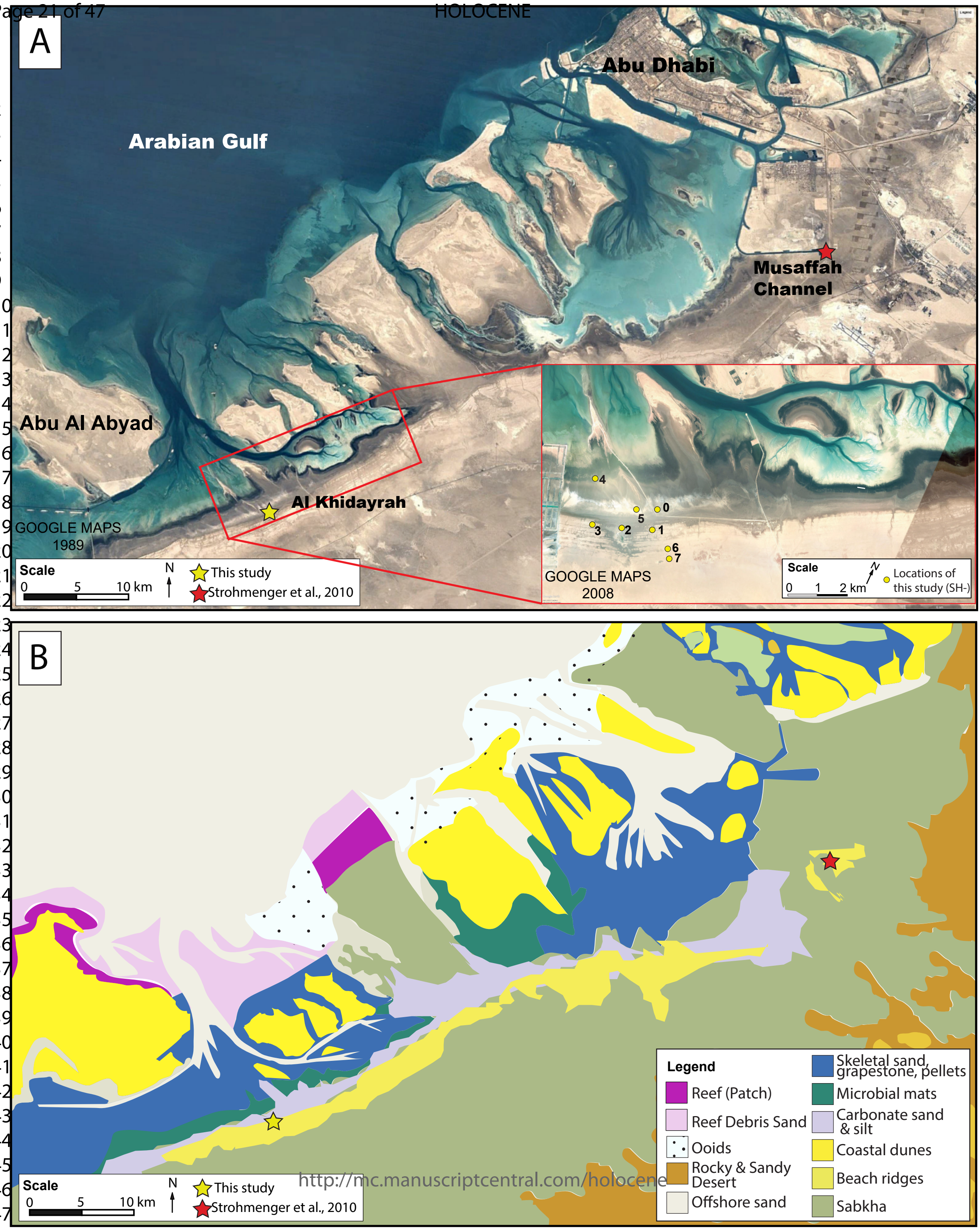
A
Abu Dhabi
Arabian Gulf
Musaffah
Channel
Abu Al Abyad
Al Khidayrah
GOOGLE MAPS
1989
Scale
0 5 10 km
N
This study
Strohmenger et al., 2010
4
0
5
3
2
1
6
7
GOOGLE MAPS
2008
Scale
0 1 2 km
Locations of
this study (SH-)
B
Legend
Reef (Patch)
Reef Debris Sand
Ooids
Rocky & Sandy
Desert
Offshore sand
Skeletal sand,
grapestone, pellets
Microbial mats
Carbonate sand
& silt
Coastal dunes
Beach ridges
Sabkha
Scale
0 5 10 km
N
This study
Strohmenger et al., 2010

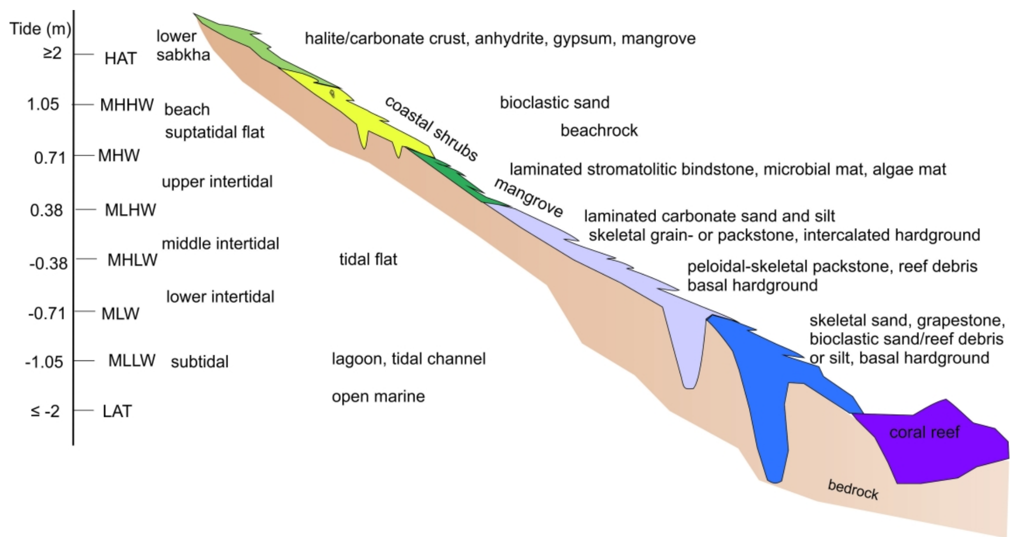

Fig. 4. Concept of facies distribution deduced from the modern analogue displayed in Figs 2 and 3 and from literature (Alsharhan and Kendall, 2003; Strohmenger et al., 2011).

294x155mm (300 x 300 DPI)

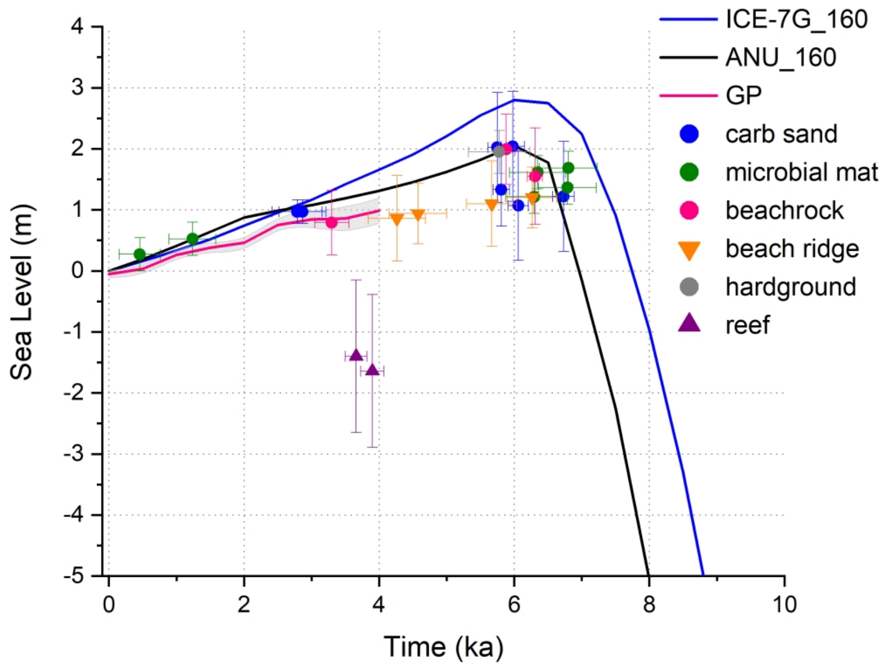

Fig. 5. Sea-level curves predicted by ICE-7G and ANU models (LT=160 km) and by the GP model compared to all proxy data

272x208mm (300 x 300 DPI)

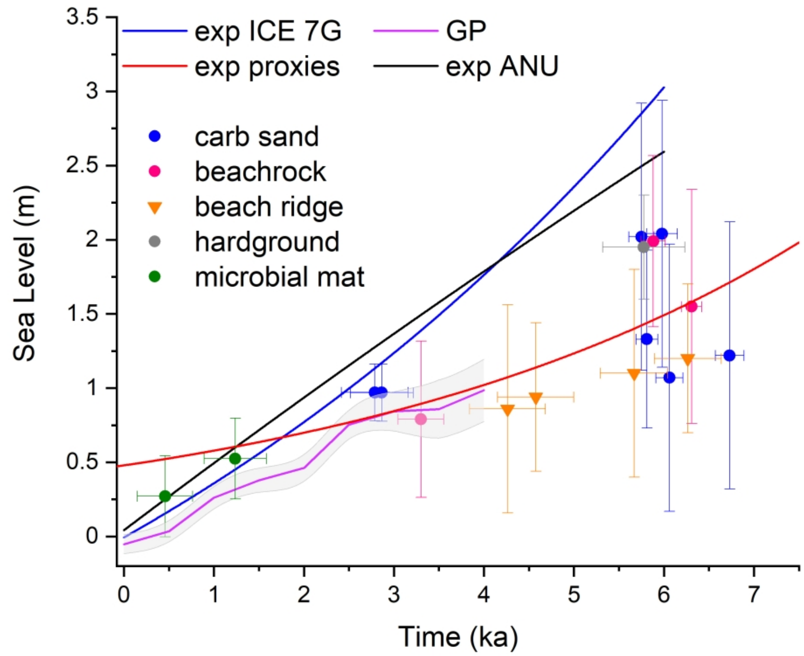

Fig. 6. The curves resulting from the exponential decay fit (exp) of ICE-7G (blue), ANU (black) and proxy data (red; data points representing transgression excluded). Gaussian Process (GP) model curve (purple) and proxy data are also plotted. For details of fits see Figs S2 and S3.

272x208mm (300 x 300 DPI)

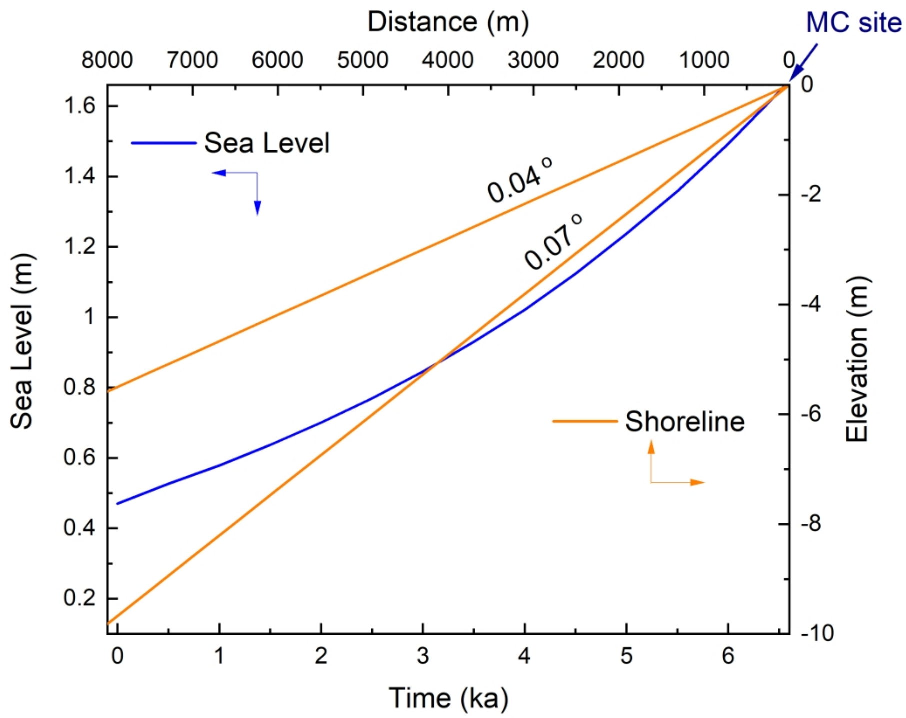

Fig. 7. The sea-level fall (blue line) and the shoreline progradation line (orange line) since the mid Holocene calculated for the MC site. At 6.7 ka the shoreline is at 0 m elevation at the MC site and then migrates seaward over a distance of 8 km following the falling sea level.

272x208mm (300 x 300 DPI)

The mid Holocene sea-level change in the Arabian Gulf

Supplement

Barbara Mauz, Zhixiong Shen, Mohammad Alsuwaidi, Daniele Mellini, Giorgio Spada, Sam J. Purkis

Fig. S1. The upper intertidal at low tide. Spade is 60 cm tall.

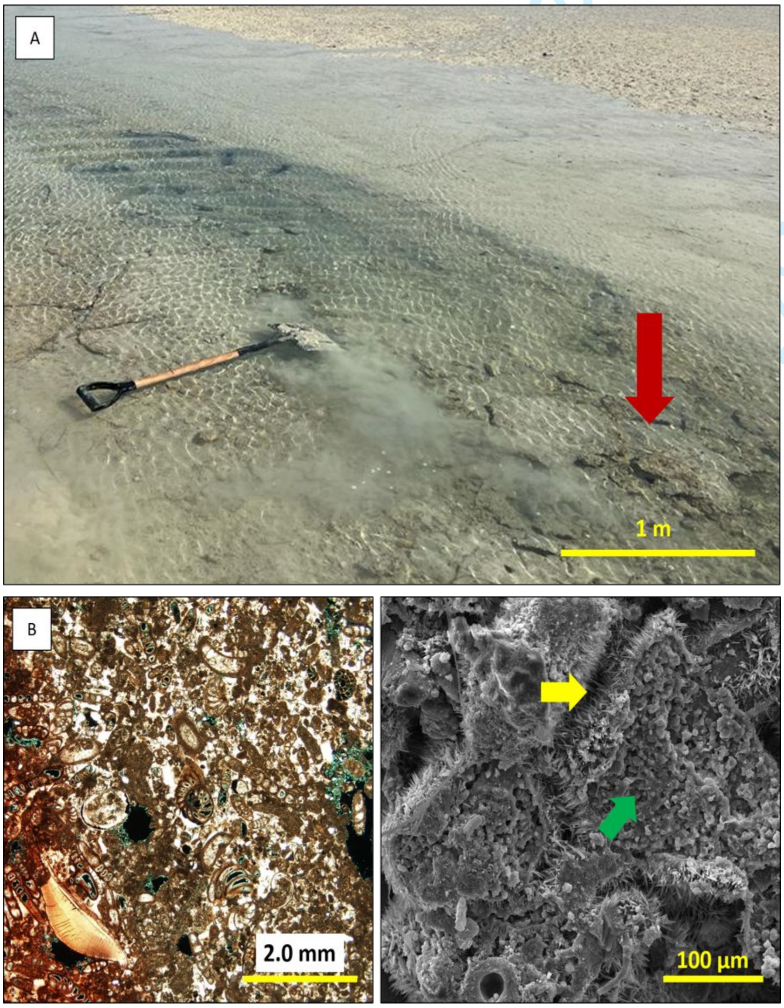

Fig. S2. A - Field photograph of the modern hardground forming in the lower intertidal to subtidal within a tidal channel, red arrow pointing at clasts of the hardground. B - thin section image (polarised light) of sample Sh 3 (Table S1) showing micritised peloids in brown colour and aragonite cement in white colour. C - SEM image of the same sample showing aragonite fibrous cement (yellow arrow) and a micritised grain (green arrow).

Table S1. Facies description of hardground (HG) using score values: 1 = <3%, 2 = 5-10%, 3 = >15%. Texture (TX) follows Dunham Classification: Fg=floatstone with grainstone matrix, Fp=Floatstone with packstone matrix, Pw= mud-dominated packstone, P= grain-dominated packstone, G= grainstone. DI: dolomitisation index, AR=aragonite cement, CCM=calcite cement, VPO (%)=visible porosity, PTY=Pore Types: I=intergranular, M=moldic, C=chamber, GS=average grain size (coarse (c), medium (m), fine (f), SO=sorting (well (w), medium (m), poor (p), PE=peloids, OO=ooid, FO=other forams, BI=bivalves, GST=gastropods, EC=echinoderms.

Sample	Location (Fig. 3a)	Description	TX	DI	AR	CCM	VPO	PTY	GS	SO	OO	PE	FO	BI	GST	EC
Sh 1	1	HG	Fg	0	3	97	35	I, M, C	M-C	M	1	3	3	2	2	1
Sh 3	5	Upper HG	Fp	0	0	100	20	I, M, C	F-M	P-M	0	2	3	2	1	1
Sh 4	0	Upper HG)	Fg	0	2	98	35	I, M, C	F-M	P-M	0	3	2	3	2	1
Sh 4.5	0	Lower HG	Fg	0	0	100	25	I, M, C	F-M	P-M	0	2	2	3	1	1
Sh 5	4	Upper HG	Fw	0	0	100	35	I, M, C	F-M	P	0	2	3	2	1	1
Sh 6	4	Lower HG	Pg	0	0	100	25	I, M, C	M	M-W	1	3	3	2	1	1
Sh 7	5	Lower HG	Pw	0	0	100	5	I, M, C	F-M	P	1	3	3	2	1	1
Sh 9	3	Upper HG	G	0	0	100	5	I, M, C	F-M	P	1	3	3	2	1	1
Sh 10	2	Upper HG	Fp	0	0	100	35	I, M, C	F-M	P	1	2	3	3	2	1
Sh 11	2	Lower HG	Fp	0	90	10	10	I, M, C	F-M	P	1	3	2	2	3	1

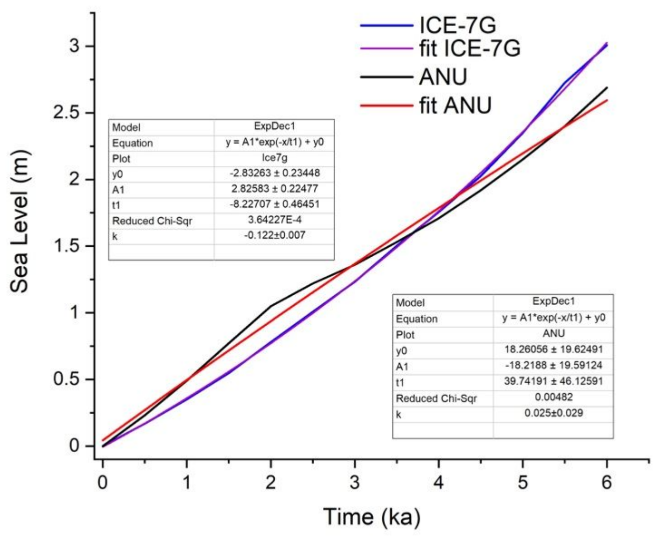

Fig. S3. The GIA-modelled sea-level curves and results from fitting these curves with the exponential decay function. See box for equation and model results where y_0=offset, a=amplitude, t=time and k=1/t (decay rate).

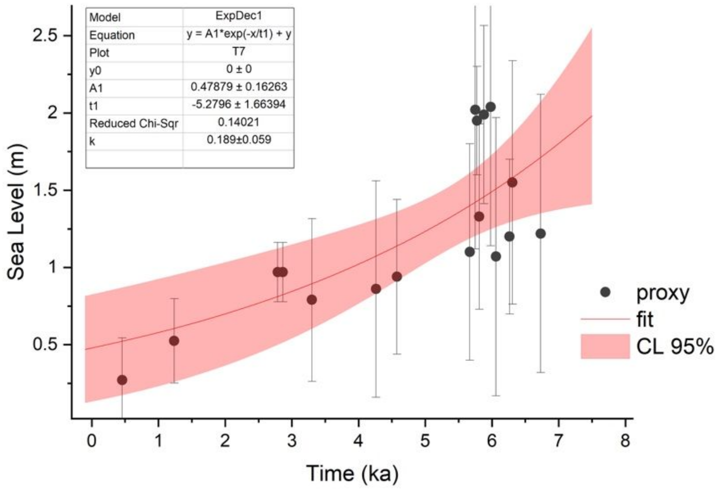

Fig. S4. The exponential decay fit and 95% confidence level of all proxy data representing the sea-level fall. To avoid over-parametrisation no error weighing performed and y_0 fixed. For description of parameters see caption of Fig S3.

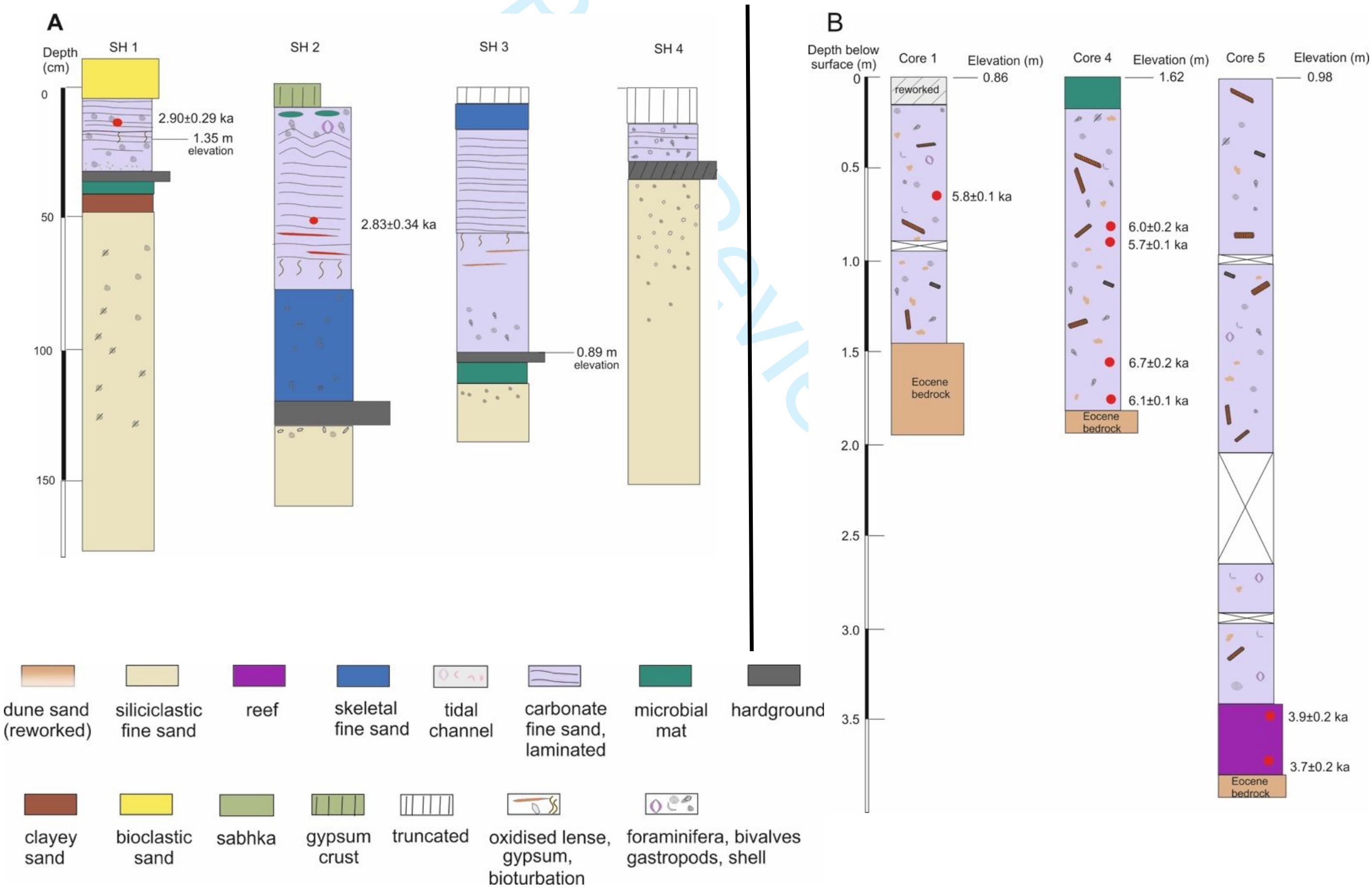

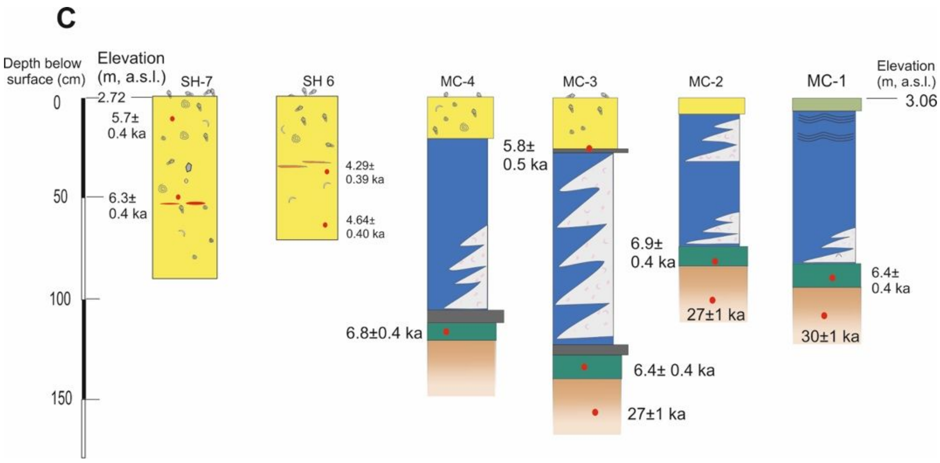

Fig. S5. Sediment succession in the sites studied; A – Al Khidayrah (SH logs; this study), B – North Qatar (Cores 1, 4 and 5; modified from Rivers et al., 2020); C - Al Khidayrah (SH logs, this study) and Mussafah Channel (MC logs; modified from Strohmenger et al., 2010).

XRF analysis and results

XRF measurements have been performed on granular samples at natural state using Niton Thermo X-ray fluorescence scanner with fully shielded test beam. The beam time was 120 seconds and each sample was measured three times. The XRF instrumental drift was corrected by measuring four certified standards in between samples: calcite in house, NIST 2709a (San Joaquin soil), SiO_2 (99%), and NIST 1D (argillaceous limestone). The results obtained were corrected using the 3 point method. The curve for each element was obtained by linear regression.

The elements that are useful for chemo-stratigraphical analysis are: (i) calcium to define episodes of high productivity, (ii) silicon to infer the siliciclastic – detrital influx, (iii) Strontium as a proxy for aragonite and (iv) Sulfur indicating gypsum and anhydrite.

The ~25% calcium and >2% Si confirm high carbonate productivity and absence of siliciclastic input. Small Ca/Sr ratios around 75 indicate the presence of aragonitic components, e.g. gastropods while high Ca/Sr ratios around 110 indicate the presence of micritised allochems. Sulfur is high in the uppermost part of the beach ridge (SH 7) where gypsum and anhydrite form today.

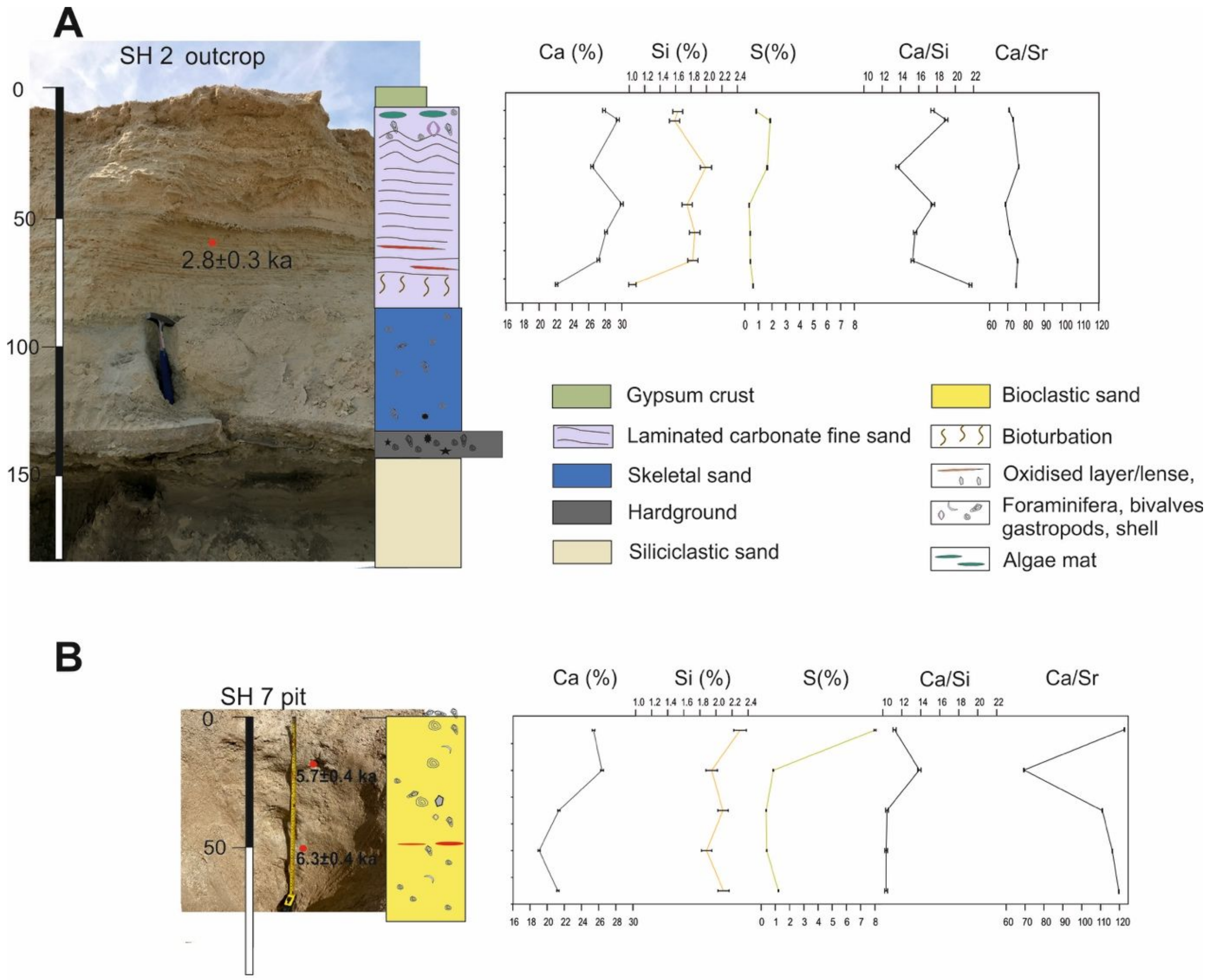

Fig. S6. The results from the XRF analysis shown for A - the SH 2 outcrop and B - the SH7 pit. Ca/Sr indicates constant (in SH 2) and variable (in SH 7) aragonite content depending on abundance of molluscs shells.

Radiocarbon dating

Radiocarbon dating was conducted on bivalves and foraminifera shells extracted from the corresponding sandy deposit following Dunbar et al. (2016). The radiocarbon ages (BP) were calibrated using the Calib 8.2 programme (Stuiver et al., 2022) and the Marine20 calibration curve (Heaton et al., 2020) and this included ΔR=76 ± 50 obtained from the Marine20 database. For increasing the number of datapoints published data were included if these meet the requirements for constraining a SLIP (see above). Wherever possible, radiocarbon ages published were re-calibrated using the method outlined above.

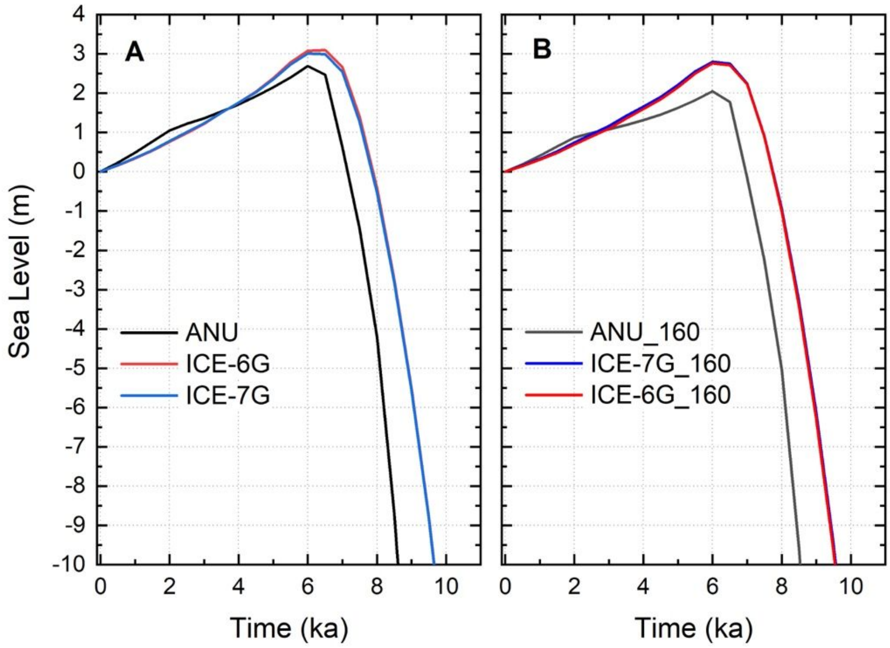

Fig. S7. Output of GIA models, A-using nominal values and B-using 160 km for lithosphere thickness.

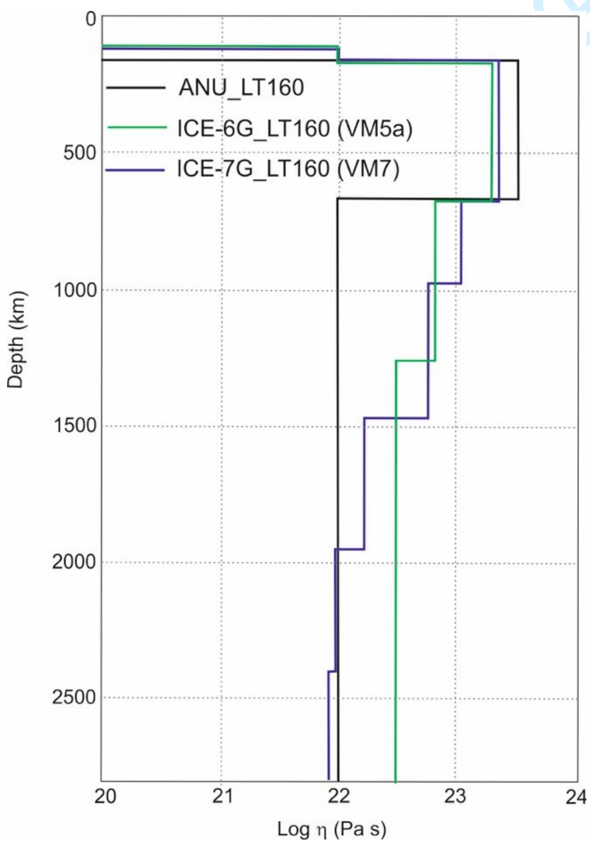

Fig. S8. Viscosity profiles employed by ANU, ICE-6G (VM5a) and ICE-7G (VM7).

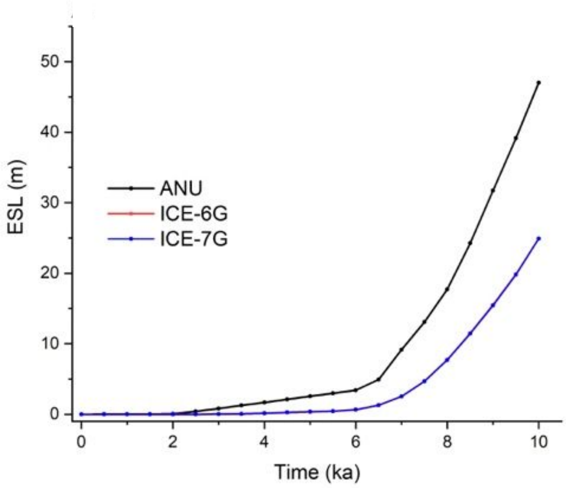

Fig. S9. The sea-level functions used in the GIA models.

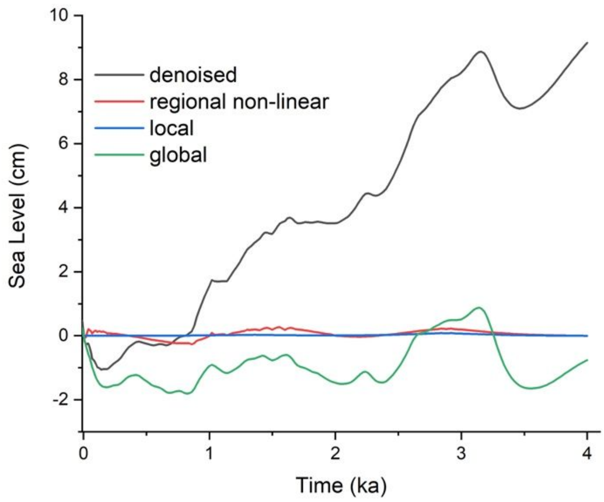

Fig. S10. The sea-level components resulting from the GP model.

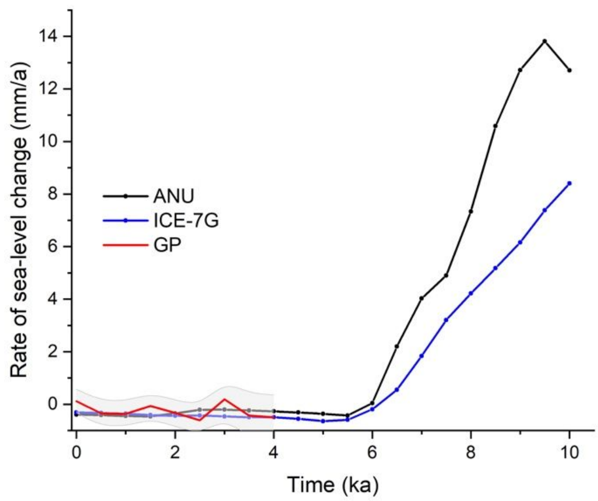

Fig. S11. Rate of sea-level change deduced from ICE-7G, ANU and GP models.

References

Dunbar, E., Cook, G.T., Naysmith, P., Tripney, B.G., and Xu, S. (2016) AMS 14C dating at the Scottish Universities Environmental Research Centre (SUERC) Radiocarbon Dating Laboratory. *Radiocarbon*, 58(01), pp. 9-23. (doi:10.1017/RDC.2015.2)

Heaton TJ, Köhler P, Butzin M, Bard E, Reimer RW, Austin WEN, Bronk Ramsey C, Hughen KA, Kromer B, Reimer PJ, Adkins J, Burke A, Cook MS, Olsen J, Skinner LC 2020. Marine20-the marine radiocarbon age calibration curve (0-55,000 cal BP).*Radiocarbon* 62. doi: 10.1017/RDC.2020.68.

Stuiver, M., Reimer, P.J., and Reimer, R.W., 2022, CALIB 8.2 [WWW program] at http://calib.org, accessed 2022-2-8.

Lab code	Field name	Depth (cm) below ground	Elevation (m, msl)	Dated material	$\delta^{13}C$ (‰)	Conventional age (BP)	err
75241	Shrimp 1R	25	1.34	Forams and bivalve shells	3.4	3277	21
75242	Shrimp 2R	68		Forams and bivalve shells	4.4	3218	21
75243	Shrimp 6UR	40	2.26	Forams and bivalve shells	4	4398	20
75244	Shrimp LR6	72	1.94	Forams and bivalve shells	3.9	4622	22
75251	Shrimp 7LR	20	2.2	Forams and bivalve shells	4.4	6113	23
75252	Shrimp 7UR	50	2.5	Forams and bivalve shells	4	5549	23
	SH 0-1	0.4		gastropod	5.3	2360	30
	SH 0-2	4.1		gastropod	3.7	6700	30
	SQ-T1-2	42		anhydrite	0.3	12860	50
	SQ-T2	95		Halite-cemented hardground	3.9	3470	70
	SQ-T3-5	50		crinkly lam microbial mat	-10.5	2190	40
	SQ-T3-2	88		aragonite Hg	-1.4	2900	70
	SQ-T4-7	3		Halite crust	-17.1	1910	40
	SQ-T4	20-32		crinkly lam microbial mat	-17.1	2090	70
	SQ-T4-2	50		aragonite Hg	0.9	2090	70
	SQ-T5-6	22		crinkly lam microbial mat	-10	1680	40
	SQ-T5-2	47		Hg	3.9	2230	60
	SQ-T6-2			crinkly lam microbial mat		1930	70
	SQ-T6-2	46		Gypsum Hg	1.2	1930	70
	SQ-T7-2	37		aragonite Hg	1.7	1280	60
	SQ-T7-3	22		crinkly lam microbial mat	-8.2	880	40
	SQ-T8-2	42		aragonite Hg	3.1	1550	60
	SQ-T9-2	28		aragonite Hg	-0.3	1320	70
UB16441	MC-2L	108		bivalve shell from Hg	1	6452	32
UB16450	MC-3L	70-95		barnacle	-4.7	5032	30
UB16451	MC-3L	70-95		bivalve *Barbatia*	-1.5	4743	27
UB16452	MC-3L	70-95		bivalve *Barbatia*	-0.8	5002	29
	MC1-4	90	2.15	microbial mat	-10.1	6180	50
	MC2-2	83	2.22	microbial mat	-10.6	6600	40
	MC3A-2	130	1.75	microbial mat	-9.9	6140	50
	MC3A-5	70	2.36	shells	0.1	6160	50
	MC3A-7	40	2.65	bulk Hg	-3.2	5660	70
	MC4-2	115	1.9	microbial mat	-10.8	6590	40
	SN-12	60		forams	2.9	6570	30

	MC1-1		170		bulk organic matter	-0.1	26760	180
	MC2-1		107		bulk organic matter	0.7	23530	140
	MC3A-1		155		bulk organic matter	0.7	24010	150
Beta-459136	Ghagha E2	subaerial sample		2.87	cerithids	not reported	not reported	
Beta-459138	Ghagha O3	subaerial sample		2.43	cerithids	not reported	not reported	
Beta-459135	Ghagha E1	subaerial sample		1.67	cerithids	not reported	not reported	
	C5-1		382	-2.84	Palygyra coral	not reported	not reported	
	C5-2		358	-2.6	Palygyra coral	not reported	not reported	
	C1-1		73	0.13	Gastropod	not reported	not reported	
	C4-1		175	-0.13	Gastropod	not reported	not reported	
	C4-2		16	0.02	Gastropod	not reported	not reported	
	C4-3		8	0.82	Gastropod	not reported	not reported	
	C4-4		78	0.84	Gastropod	not reported	not reported	
385711	AZ-W5/19F		422	-4.3	bivalve	3.3	5670	30
414136	AZ-W7/21F		643	-5.9	bivalve, articulated	2.4	5290	30
396443	AZ-W9/12F		180	-0.8	bivalve	2.6	4330	30
UB7041	Site01-B39		42		microbial mat	-7	1933	33
UB7474	Site10-S143		35.5		microbial mat	-10	1096	29

Calibrated age (AD/BC)	Calibrated age (AD/BC)	cal ka uppe	cal ka lower	cal BP	err	Reference
1090	741	3040	2691	2865.5	349	this study
1023	651	2973	2601	2787	372	this study
2524	2102	4474	4052	4263	422	this study
2838	2414	4788	4364	4576	424	this study
4500	4128	6450	6078	6264	372	this study
3905	3530	5855	5480	5667.5	375	this study
422	37	2372	1987	2179.5	385	Paul and Lokier 17
5189	4773	7139	6723	6931	416	Paul and Lokier 17
12802	12102	14752	14052	14402	700	S et al 2011
1262	997	3212	2947	3079.5	265	S et al 2011
618	241	1332	1709	1520.5	-377	S et al 2011
727	194	2677	2144	2410.5	533	S et al 2011
906	553	1044	1397	1220.5	-353	S et al 2011
746	301	1950	1649	1799.5	301	S et al 2011
746	301	2696	2251	2473.5	445	S et al 2011
1154	772	796	1178	987	-382	S et al 2011
603	163	2553	2113	2333	440	S et al 2011
922	475	1028	1475	1251.5	-447	S et al 2011
922	475	1028	1475	1251.5	-447	S et al 2011
1500	1164	450	786	618	-336	S et al 2011
1885	1501	65	449	257	-384	S et al 2011
1283	894	667	1056	861.5	-389	S et al 2011
1474	1098	476	852	664	-376	S et al 2011
4885	4476	6835	6426	6630.5	409	Lokier etal 15
3329	2909	5279	4859	5069	420	Lokier etal 15
2942	2535	4892	4485	4688.5	407	Lokier etal 15
3308	2887	5258	4837	5047.5	421	Lokier etal 15
4602	4188	6552	6138	6345	414	Strohmenger et al 2010
5065	4636	7015	6586	6800.5	429	Strohmenger et al 2010
4557	4134	6507	6084	6295.5	423	Strohmenger et al 2010
4579	4161	6529	6111	6320	418	Strohmenger et al 2010
4054	3598	6004	5548	5776	456	Strohmenger et al 2010
5051	4623	7001	6573	6787	428	Strohmenger et al 2010
5019	4611	6969	6561	6765	408	S and J 2018

28562	27697	30512	29647	30079.5	865	Strohmenger et al 2010
25236	24480	27186	26430	26808	756	Strohmenger et al 2010
25690	25046	27640	26996	27318	644	Strohmenger et al 2010
		6015	5745	5880	135	Damien et al 2020
		6420	6195	6307.5	112	Damien et al 2020
				3300	255	Damien et al 2020
				3900	170	Rivers et al. 2020
				3660	160	Rivers et al. 2020
				5810	120	Rivers et al. 2020
				6060	150	Rivers et al. 2020
				6730	160	Rivers et al. 2020
				5750	140	Rivers et al. 2020
				5980	170	Rivers et al. 2020
4009	3640	6009	5590	5799.5	319	Engel et al. 2021
3627	3255	5577	5205	5391	372	Engel et al. 2021
2445	2008	4395	3958	4176.5	437	Engel et al. 2021
886	541	1064	1409	1236.5	345	Lokier and Steuber 2008
1647	1340	303	610	456.5	307	Lokier and Steuber 2008

no elevation data
no elevation data
no elevation data
no elevation data
no elevation data
no elevation data
no elevation data
no elevation data
no elevation data
no elevation data
no elevation data
no elevation data
no elevation data
no elevation data
recent microbial mat facies belt
recent microbial mat facies belt
no elevation data
no elevation data
no elevation data
no elevation data
elevation measured in this study
elevation measured in this study
elevation measured in this study
transported
elevation measured in this study
elevation measured in this study
no elevation data

elevation measured in this study
elevation measured in this study
elevation measured in this study

large IR of beachrock as indicator

Marine 13 and Southon et al 2002 for ΔR

Gastropod not in situ

Gastropod not in situ

Gastropod not in situ

Gastropod not in situ

Gastropod not in situ

	lat	long	elevation m)	mean elev
test1	24∞04'07.62557"N	54∞02'32.88406"E	3.107	
shrimp-6INT	24∞06'27.43885"N	54∞04'00.04670"E	2.013	
shrimp-6INT2	24∞06'27.43614"N	54∞04'00.04721"E	2.01	2.0115
shrimp-0HG	24∞07'06.09821"N	54∞03'21.11303"E	0.567	
shrimp-0HG1	24∞07'06.09845"N	54∞03'21.11279"E	0.557	0.562
shrimp-1INT	24∞06'41.12118"N	54∞03'26.10982"E	1.347	
shrimp-1INT1	24∞06'41.12140"N	54∞03'26.10975"E	1.352	1.3495
shrimp-5HG	24∞06'56.16932"N	54∞02'54.91668"E	0.394	
shrimp-5HG1	24∞06'56.16938"N	54∞02'54.91714"E	0.405	0.3995
shrimp-3HG	24∞06'18.84754"N	54∞02'13.15113"E	0.888	
shrimp-3HG1	24∞06'18.84769"N	54∞02'13.15100"E	0.895	0.8915
shrimp-4HG	24∞07'09.43329"N	54∞01'52.27099"E	-0.029	
shrimp-4HG1	24∞07'09.43277"N	54∞01'52.27062"E	-0.02	-0.0245
shrimp-7INT1	24∞06'11.85558"N	54∞04'02.61227"E	2.718	
shrimp-7INT	24∞06'11.85560"N	54∞04'02.61190"E	2.715	2.7165
MC1	24∞18'875"N	54∞31'536"E	2.88	
MC2	24∞18'844"N	54∞31'538"E	3.039	
MC3	24∞18'849"N	54∞31'538"E	3.235	3.0513333
Benchmark ID3197	24.2782	54.522	6.042	

err
0.03
0.03
0.03
0.1
0.07
0.03
0.04
0.04

Sample field name	GPS	long (E decimal)	lat (N, decimal)	Elevation (m, msl)	elevation err	Calibrated age (ka) (2σ)	± ka
Shrimp 1R	shrimp-1INT	54.05722222	24.11142255	1.3495	0.03	2.866	0.349
Shrimp 2R	shrimp-2INT	54.04694444	24.10776667	1.350	0.03	2.787	0.372
Shrimp 6UR	shrimp-6INT	54.06666667	24.1076219	2.260	0.03	4.263	0.422
Shrimp 6LR	shrimp-6INT	54.06666667	24.1076219	1.940	0.03	4.576	0.424
Shrimp 7LR	shrimp-7INT	54.06722222	24.10329167	2.200	0.04	6.264	0.372
Shrimp 7UR		54.06722222	24.10329167	2.500	0.04	5.668	0.375
MC1-4		55.29111111	24.31211667	2.150	0.03	6.345	0.414
MC2-2		55.29111111	24.31211667	2.22	0.03	6.801	0.429
MC3A-2		55.29111111	24.31211667	1.75	0.03	6.296	0.423
MC3A-7		55.29111111	24.31211667	2.65	0.03	5.776	0.456
MC4-2		55.29111111	24.31211667	1.9	0.03	6.787	0.428
C5-1		51.275	26.158333	-2.84	0.02	3.900	0.170
C5-2		51.275	26.158333	-2.6	0.02	3.660	0.160
C1-1		51.2575	26.1491666	0.13	0.02	5.810	0.120
C4-1		51.273611	26.14444	-0.13	0.02	6.060	0.150
C4-2		51.273611	26.14444	0.02	0.02	6.730	0.160
C4-3		51.273611	26.14444	0.82	0.02	5.750	0.140
C4-4		51.273611	26.14444	0.84	0.02	5.980	0.170
G03		51.5534	24.4115	2.43	0.243	6.308	0.112
Ge2		51.5534	24.4115	2.87	0.287	5.880	0.135
Ge1		51.5534	24.4115	1.67	0.167	3.300	0.255
Site01-B39	shrimp-5HG	54.028	24.1166	-0.0205	0.00082	1.237	0.345
Site10-S143	shrimp-4HG	54.0119	24.1131	-0.2745	0.01098	0.457	0.307

Sed Description	Depos environ	Thickness (cm)	Strat/Sampling Info	IR (m)	IR/2 (m)	RWL
laminated carb sand	mid intertidal	25	20 cm below sabkha surface	0.38	0.19	MSL
lam carb sand	mid int	24	58 cm below halite cru	0.38	0.19	MSL
bioclastic sand	beach ridge	83	40 cm below surface	1.4	0.7	MSL
bioclastic sand	beach ridge (bottom)	83	72 cm below surface	1	0.5	MSL
bioclastic sand	beach ridge (bottom)	60	50 cm below surface	1	0.5	MSL
bioclastic carb sand	beach ridge	60	20 cm below surface	1.4	0.7	MSL
crinkly-laminated microbial mat	upp int	11	directly overlying terr Pleistocene sand	0.545	0.2725	MSL
crinkly-laminated microbial mat	upp int	11	directly overlying terr Pleistocene sand	0.545	0.2725	MSL
crinkly-laminated microbial mat	upp int	11	directly overlying terr Pleistocene sand	0.545	0.2725	MSL
Hg	upp int	2	above micro mat	0.7	0.35	MSL
crinkly-laminated microbial mat	upp int	11	directly overlying terr Pleistocene sand	0.545	0.2725	MSL
reef	upp-mid subtidal	30	coral reef colonising bedrock	2.5	1.25	MSL
reef	upp-mid subtidal	30	coral reef colonising bedrock	2.5	1.25	MSL
packstone	intertidal	120	continuous intertidal carb sand	1.2	0.6	MSL
grainstone	intertidal	180	continuous intertidal carb sand	1.8	0.9	MSL
grainstone	intertidal	180	continuous intertidal carb sand	1.8	0.9	MSL
grainstone	intertidal	180	continuous intertidal carb sand	1.8	0.9	MSL
grainstone	intertidal	180	continuous intertidal carb sand	1.8	0.9	MSL
beachrock	beach/supra tidal	not reported	10m from modern coastline	1.5	0.75	MSL
beachrock	beach/supra tidal	not reported	rim of flooded depression, calm, low tidal range	1	0.5	MSL
beachrock	beach/supra tidal	not reported	rim of flooded depression, calm, low tidal range	1	0.5	MSL
microbial mat	upp int	8	close to modern shoreline	0.545	0.2725	MSL
microbial mat	upp int	18	close to modern shoreline	0.545	0.2725	MSL

Palaeo-mean sea level	±	Type of indicator	Reference	Eleveation measurement technique
0.970	0.192	SLIP	this study	dGPS
0.970	0.192	SLIP	this study	dGPS
0.860	0.701	terr limiting	this study	dGPS
0.940	0.501	terr limiting	this study	dGPS
1.200	0.502	terr limiting	this study	dGPS
1.100	0.701	SLIP	this study	dGPS
1.605	0.274		Strohmenger et al 2010	dGPS
1.675	0.274		Strohmenger et al 2010	dGPS
1.205	0.274		Strohmenger et al 2010	dGPS
1.950	0.351		Strohmenger et al 2010	dGPS
1.355	0.274		Strohmenger et al 2010	dGPS
-1.640	1.250	marine lim	Rivers et al., 2020	dGPS
-1.400	1.250	marine lim	Rivers et al., 2020	dGPS
1.330	0.600	SLIP	Rivers et al., 2020	dGPS
1.070	0.900		Rivers et al., 2020	dGPS
1.220	0.900		Rivers et al., 2020	dGPS
2.020	0.900		Rivers et al., 2020	dGPS
2.040	0.900		Rivers et al., 2020	dGPS
1.550	0.788		Damien et al. 2020	clinometer uncertainty set to 10%
1.990	0.577		Damien et al. 2021	clinometer uncertainty set to 10%
0.790	0.527		Damien et al. 2022	clinometer uncertainty set to 10%
0.525	0.273		Lokier and Steuber 2008	benchmarked to modern microbi
0.271	0.273		Lokier and Steuber 2008	benchmarked to modern microbi

%

%

%

ial mat

ial mat

Site/Sample	Lat	Long	Time (ka before	± (ka)	± (%)	Sea Level (m	± (m)
SH1	24.11142	54.05722	2.866	0.349	12.179	0.970	0.192
SH2	24.10777	54.04694	2.787	0.372	13.348	0.970	0.192
SH6U	24.10762	54.06667	4.263	0.422	9.899	0.860	0.701
SH6L	24.10762	54.06667	4.576	0.424	9.266	0.940	0.501
SH7L	24.10329	54.06722	6.264	0.372	5.939	1.200	0.502
SH7U	24.10329	54.06722	5.668	0.375	6.617	1.100	0.701
MC1-4	24.31212	55.29111	6.345	0.414	6.525	1.605	0.274
MC2-2	24.31212	55.29111	6.801	0.429	6.308	1.675	0.274
MC3A-2	24.31212	55.29111	6.296	0.423	6.719	1.205	0.274
MC3A-7	24.31212	55.29111	5.776	0.456	7.895	1.950	0.351
MC4-2	24.31212	55.29111	6.787	0.428	6.306	1.355	0.274
C5-1	26.15833	51.275	3.900	0.170	4.359	-1.640	1.250
C5-2	26.15833	51.275	3.660	0.160	4.372	-1.400	1.250
C1-1	26.14917	51.2575	5.810	0.120	2.065	1.330	0.600
C4-1	26.14444	51.27361	6.060	0.150	2.475	1.070	0.900
C4-2	26.14444	51.27361	6.730	0.160	2.377	1.220	0.900
C4-3	26.14444	51.27361	5.750	0.140	2.435	2.020	0.900
C4-4	26.14444	51.27361	5.980	0.170	2.843	2.040	0.900
G03	24.4115	51.5534	6.308	0.112	1.776	1.550	0.788
Ge2	24.4115	51.5534	5.880	0.135	2.296	1.990	0.577
Ge1	24.4115	51.5534	3.300	0.255	7.727	0.790	0.527
Site01-B39	24.1166	54.028	1.237	0.345	27.901	0.525	0.273
Site10-S143	24.1131	54.0119	0.457	0.307	67.251	0.271	0.273

± (%)	Quality	Indicator	Ref
19.841	SLIP	mid intertidal carb sand	this study
19.830	SLIP	mid intertidal carb sand	this study
81.470	terr limiting	beach ridge	this study
53.287	terr limiting	beach ridge bottom	this study
41.800	terr limiting	beach ridge bottom	this study
63.740	terr limiting	beach ridge	this study
17.081	SLIP	microbial mat	Strohmenger et al 2010
16.367	SLIP	microbial mat	Strohmenger et al 2010
22.751	SLIP	microbial mat	Strohmenger et al 2010
18.015	SLIP	hardground	Strohmenger et al 2010
20.232	SLIP	microbial mat	Strohmenger et al 2010
76.229	marine lim	reef	Rivers et al 2020
89.297	marine lim	reef	Rivers et al 2020
45.138	SLIP	intertidal carb sand	Rivers et al 2020
84.133	SLIP	intertidal carb sand	Rivers et al 2020
73.789	SLIP	intertidal carb sand	Rivers et al 2020
44.565	SLIP	intertidal carb sand	Rivers et al 2020
44.129	SLIP	intertidal carb sand	Rivers et al 2020
50.863	SLIP	beachrock	Damien et al 2020
28.971	SLIP	beachrock	Damien et al 2020
66.728	SLIP	beachrock	Damien et al 2020
51.954	SLIP	microbial mat	Lokier and Steuber 2008
100.821	SLIP	microbial mat	Lokier and Steuber 2008